Monte-Carlo based quantification of uncertainties in determining ocean remote sensing reflectance from underwater fixed-depth radiometry measurements

Agnieszka Białek*

National Physical Laboratory, Teddington, TW11 0LW, UK

Vincenzo Vellucci

Sorbonne Université, CNRS, Institut de la Mer Villefranche, IMEV, F-06230 Villefranche-sur-Mer, France.

Bernard Gentili

Sorbonne Université, UPMC Univ Paris 06, INSU-CNRS, Laboratoire d'Océanographie de Villefranche, 06230, Villefranche-sur-mer, France.

David Antoine

Remote Sensing and Satellite Research Group, Department of Physics & Astronomy, Curtin University, Perth, WA 6845, Australia.

Sorbonne Université, UPMC Univ Paris 06, INSU-CNRS, Laboratoire d'Océanographie de Villefranche, 06230, Villefranche-sur-mer, France.

Javier Gorroño

National Physical Laboratory, Teddington, TW11 0LW, UK.

Nigel Fox

National Physical Laboratory, Teddington, TW11 0LW, UK.

Craig Underwood

Surrey Space Cenrte, University of Surrey, Guilford, GU2 7XH, UK.

Corresponding author address: National Physical Laboratory, Hampton Road, Teddington, TW11 0LW, UK.

E-mail: agnieszka.bialek@npl.co.uk

ABSTRACT

A new framework that enables evaluation of the *in-situ* Ocean Color Radiometry (OCR) measurement uncertainty is presented. The study was conducted on the multispectral data from a permanent mooring deployed in clear open ocean water. The uncertainty is evaluated for each component of the measurement equation and data processing step that leads to deriving the remote sensing reflectance, R_{rs}. The Monte Carlo Method (MCM) was selected to handle the data complexity such as correlation and non-linearity in an efficient manner. The results are presented for a pre-screened data set that is suitable for System Vicarious Calibration applications. The framework provides uncertainty value per measurement taking into consideration environmental conditions present during acquisition. A summary value is calculated from the statistics of the individual uncertainties per each spectral channel. This summary value is below 4 %, $(k = 1)$ for the blue and green spectral range. For the red spectral channels, the summary uncertainty value increases to approximately 5 %. The presented method helps to understand the significance of various uncertainty components and provide a way of identifying major contributors. This can be used for efficient system performance improvement in the future.

1. Introduction

Geophysical products derived from satellite remote sensing observations are now available from multiple missions, covering most compartments of the Earth system, such as the atmosphere, open oceans, coastal zones, forests and ice sheets. For a few decades, the satellite-derived geophysical variables describing these environments have been essentially used for scientific purposes, yet they are now increasingly feeding operational monitoring program (e.g., Schulz et al. 2009; Traon et al. 2015) and services to Governments, industry or the public (Zhao et al. 2005; Lafaye 2017; Harvey et al. 2015).

In both contexts, users not only require significant suites of products describing their targeted environment but also expect uncertainties to come along with these products. These uncertainties are no longer only required as generic values supposedly representative of an average uncertainty for a given sensor and associated data processing algorithms. They are often now required at the level of individual measurements (pixels). They are of paramount importance when aiming at merging data sets (Gregg and Rousseaux 2014), quantifying long-term trends (Henson et al. 2010; Saulquin et al. 2013), assimilating data into models (Mélin et al. 2016), or still when triggering warnings related to environment monitoring (Rogers et al. 2018).

Satellite ocean color radiometry (OCR) is specifically addressed here. In this case, a prerequisite to deriving geophysical product uncertainties is that uncertainties have been assigned to the quantity from which these products are derived. This quantity is the remote-sensing reflectance, $R_{\rm rs}$, derived from the water-leaving radiance, $L_{\rm w}$, in a number of spectral bands across the near ultraviolet to visible range. $L_{\rm w}$ is generally less than 10 % of the total radiance measured by the sensor at the top of the atmosphere (TOA), and actually often around 5 % only. It was demonstrated that, in such circumstances, achieving a 5 % uncertainty on $L_{\rm w}$ in the blue part of the spectrum, which

is a requirement set up rather early in the era of satellite OCR (Gordon and Clark 1981), was impossible without introducing what is now called a system vicarious calibration (SVC) (Gordon and Castaño 1987; Gordon 1997, 1998). The SVC process consists in adjusting the spectral calibration coefficients of the satellite sensors through minimizing differences between the observed TOA total radiances and equivalent modeled values. These modeled values are built from *in-situ* measurements performed in the best possible conditions combined to atmospheric radiances modeled consistently with the satellite processing algorithms. This adjustment is not only needed because of possibly imperfect calibration of the sensor but also because of unavoidable errors in the atmospheric correction process, by which the dominant part of the signal is quantified in order to eventually get to L_{w}. This is why it is referred to as a System VC.

To sustain SVC for ocean color sensors (OC-SVC in the following), the solution of deploying permanent moorings in clear open ocean waters has been adopted in the last two decades. The two currently active sites are the Marine Optical Buoy (MOBY; Clark et al. 1997) and the Bouée pour l'acquisition de Séries Optiques á Long termE (BOUSSOLE; Antoine et al. 2006). MOBY is deployed off Lanai (Hawaii) and currently supported by the US National Oceanic and Atmospheric Administration (NOAA) and used for all US ocean color missions including the Moderate Resolution Imaging Spectroradiometer (MODIS; Salomonson et al. 1989) and the Sea-viewing Wide Field-of-view Sensor (SeaWiFS; Hooker et al. 1992). BOUSSOLE is deployed in the Mediterranean Sea and currently supported by the European Space Agency (ESA) and French Centre National d'Etudes Spatiales (CNES) and used for the European missions MEdium Resolution Imaging Spectrometer (ENVISAT/MERIS; Rast et al. 1999) and Ocean and Land Colour Imager (S3A-B /OLCI; Donlon et al. 2012). Until recently, data from these two programs were provided to space agencies with a nominal combined standard uncertainty, supposedly representative of average measurement conditions for the SVC data set. It was provided for several spectral

bands for MOBY (Brown et al. 2007), and as a single number for BOUSSOLE (Antoine et al. 2008b).

The need for a more thorough estimation of uncertainties has, however, become obvious for these crucial *in-situ* measurements to be qualified for being used for OC-SVC. The goal is eventually to assign an uncertainty value to each and every measurement that the field platform provides, so that data can be selected using specific thresholds corresponding to the maximum acceptable uncertainty for various purposes. It is also to have a means of identification and correction of systematic contributions. For OC-SVC, only the data with the lowest uncertainty would be considered. Achieving this objective means that all possible sources of uncertainties are identified, individually quantified, and then combined into a single uncertainty value for each measurement. Deriving this final number is challenging, because it has to combine many uncertainty contributors of which some might be correlated. The often-used first order approximation of the Law of Propagation of Uncertainties (JCGM100 2008), commonly known as quadratic sum of individual uncertainty values is not applicable in this situation.

This paper precisely proposes another approach (JCGM101 2008), which uses a Monte Carlo Method (MCM). The process involves assigning a probability distribution function (PDF) to each identified uncertainty source, either via statistical analysis of relevant data for (type A) uncertainties, or via other non-statistical ways for (type B) uncertainties, e.g., manufacturers specifications or a priori knowledge from literature. These uncertainty sources are explicitly introduced into the measurement equation, which is then run multiple times by randomly selecting values in the PDFs of all uncertainty sources.

In the following, we start with reminding how the remote-sensing reflectance is derived from in-water radiometry measurements, and then we go through identification and quantification of uncertainty sources related to the instruments and data processing. We then present how the MCM is

used to combine uncertainties, and finally we provide an example of application where a subset of BOUSSOLE data is selected following quality criteria that qualify them as a priori suitable for OC-SVC. It is important to note that we do not intend here to propose a thorough and final uncertainty evaluation for the radiometry measurements and derived quantities at BOUSSOLE. We rather use BOUSSOLE as a test bench to demonstrate the methodology. We deliberately ignore a number of uncertainty sources, for instance, when further work is actually still needed to adequately quantify them. We also do not necessarily go through a detailed and fully justified derivation of the PDFs of individual type B uncertainties because, again, this paper is a demonstration of the method, not a provision of a full uncertainty quantification for remote sensing reflectance derived from BOUSSOLE measurements. Finally some known sources of errors are not corrected in the current version of the processing, thus they are treated and propagated as uncertainties according to GUM recommendations for relatively small biases.

2. Deriving R_{rs} from radiometric quantities measured at fixed depths

a. Basic quantities and equations

The upper-ocean apparent optical property (AOP) for which measurements uncertainties are to be quantified is the remote sensing reflectance, R_{rs}. It is defined as (here omitting wavelength and angular dependencies):

$$R_{\mathrm{rs}} = \frac{L_{\mathrm{w}}}{E_{\mathrm{s}}} \left[\mathrm{sr}^{-1}\right] , \tag{1}$$

where L_{w} is the water-leaving radiance and E_{s} the downward irradiance just above the sea surface. L_{w} is calculated according to:

$$L_{\mathrm{w}} = L_{\mathrm{u}}(0^{-})\frac{1-\rho}{n^2}\ \left[\mu\mathrm{W cm^2 nm^{-1} sr^{-1}}\right], \tag{2}$$

where $L_{\mathrm{u}}(0^{-})$ is the upwelling radiance just beneath the sea surface, ρ is the Fresnel reflection coefficient for the water-air interface and n is the refractive index of seawater. The ratio in Eq. 2 is often given the approximate value of 0.543 (Austin 1974; Mueller et al. 2003). When underwater measurements are taken at two fixed depths, $L_{\mathrm{u}}(0^{-})$ is determined through:

$$L_{\mathrm{u}}(0^{-}) = L_{\mathrm{u},z_{\mathrm{u}}} exp(K_{L_{\mathrm{u}}} z_{\mathrm{u}})\ \left[\mu\mathrm{W cm^2 nm^{-1} sr^{-1}}\right], \tag{3}$$

where $L_{\mathrm{u},z_{\mathrm{u}}}$ is the upwelling radiance at the shallowest (upper) measurement depth z_{u}, and $K_{L_{\mathrm{u}}}$ is the diffuse attenuation coefficient for upwelling radiance, itself computed as:

$$K_{L_{\mathrm{u}}} = -\frac{\ln(L_{\mathrm{u},z_{\mathrm{l}}}/L_{\mathrm{u},z_{\mathrm{u}}})}{(z_{\mathrm{l}} - z_{\mathrm{u}})}\ \left[\mathrm{m^{-1}}\right], \tag{4}$$

where $L_{\mathrm{u},z_{\mathrm{l}}}$ is the upwelling radiance at the deepest (lower) measurement depth, i.e. $z_{\mathrm{l}} > z_{\mathrm{u}}$. Although the above equations are valid for any zenith angle included into the Snells cone, we here consider the specific case of upwelling radiances at nadir. Quantifying uncertainties on R_{rs} means quantifying uncertainties i) on the measurement of the relevant radiometric quantities, here $L_{\mathrm{u},z_{\mathrm{u}}}$, $L_{\mathrm{u},z_{\mathrm{l}}}$ and E_{s}, and depth ii) on their propagation through Eq. 4 to calculate $K_{L_{\mathrm{u}}}$, and iii) on the transmission across the water-air interface (Eq. 2). Combining Eq. 2 to Eq. 4 leads to the full measurement equation below.

$$R_{\mathrm{rs}} = \frac{L_{\mathrm{u},z_{\mathrm{u}}} exp\left(-\frac{ln(L_{\mathrm{u},z_{\mathrm{l}}}/L_{\mathrm{u},z_{\mathrm{u}}})}{z_{\mathrm{l}} - z_{\mathrm{u}}} z_{\mathrm{u}}\right)\left(\frac{1-\rho}{n^2}\right)}{E_{\mathrm{s}}}\ \left[\mathrm{sr^{-1}}\right]. \tag{5}$$

The practical realization in the case of the BOUSSOLE buoy is shown in a schematic way on Fig. 1, with $z_{\mathrm{u}} = 4$ m, $z_{\mathrm{l}} = 9$ m. Therefore, from now on $L_{\mathrm{u}4}$ and $L_{\mathrm{u}9}$ will be used to represent

the upwelling radiances at nominal depths of 4 m and 9 m, respectively (instead of L_{u,z_u} and L_{u,z_l}). The BOUSSOLE buoy was designed to be stable, so the depths z_u and z_l vary in a rather limited range (Antoine et al. 2008a).

b. Instruments used

Three multispectral radiometers of the Satlantic 200 series are used to measure L_{u4}, L_{u9} and E_s. They have seven spectral channels at 412, 443, 490, 510, 555, 670 and 683 nm, each with a 10 nm bandwidth. The measurements are taken simultaneously every fifteen minutes throughout the day and night, as one-minute measurement sequences. These radiometers have a 6 Hz frequency of acquisition, resulting in 360 measurements during each sequence. Night measurements are used as dark readings. They allow monitoring of possible drift in instrument noise levels during a deployment. BOUSSOLE functions on an approximately 6-month servicing schedule, with successive rotations on site between a calibrated and verified buoy and the buoy having been deployed for the previous 6 months or so. Therefore, two full sets of radiometers are successively used. Additional instruments on the buoy that are used as an ancillary data source for the processing include a two-axis tilt and compass sensor (Advanced Orientation Systems EZ-III) and a Conductivity Temperature Depth (CTD) sensor (Sea-Bird Scientific 37-SI). Both sensors are attached to the main buoy structure at 9 m depth. Meteorological data including wind direction and speed and atmospheric pressure are taken from a meteorological buoy that is deployed two nautical miles away from the BOUSSOLE site.

3. Instruments characterization and calibration uncertainties

In the following sections, the derivation of uncertainty values corresponding to various steps of the characterization and calibration of instruments is described. Important parameters of these

uncertainties are the best estimate (e.g. average typical value) and their Probability Distribution Functions (PDF). Both are going to be used when combining all uncertainties via the Monte Carlo Method (MCM), which is described later on.

a. Absolute calibration

Since the beginning of BOUSSOLE operations, absolute radiometric calibration is undertaken about once a year for each set of radiometers, before they go at sea for a 6- to 9-month deployment. This calibration is performed at the manufacturers grounds (previously Satlantic Inc., Halifax, Canada, since 2018 Sea Bird Scientific, Bellevue, USA). During that time any necessary instrument reparations are carried out. The absolute radiometric calibration coefficients are provided, yet they are not accompanied by what would be the uncertainty of the calibration process. In 2012, one set of BOUSSOLE radiometers was sent to the UKs National Measurements Institute (National Physical Laboratory, NPL) for calibration and characterization tests, as a first step towards establishing an uncertainty budget for their absolute calibration. The difference between NPL- and Satlantic-derived calibration coefficients, combined with the NPL laboratory calibration uncertainty values (previously evaluated including all effects that are associated with the calibration process, such as the lamp current, ageing and uniformity effects as well as alignment, instrument reading stability and reflectance panel uniformity), form the radiometric calibration uncertainty used in this work. These derived uncertainty values are presented in Table 1 per spectral channel for irradiance and radiance.

The uncertainties in absolute radiometric calibration have a normal distribution with the mean of the multiplicative correction factor equal to 1. The standard deviation of this distribution is equal to the absolute calibration uncertainty combined with the uncertainty related to the stability of this calibration, $u(\text{stab})$, a priori set here at 1 % (Eq. 6). The stability has a rectangular distribution

and before being combined with the calibration uncertainty is divided by the square root of three to provide a value corresponding to a normal distribution.

$$u(\mathrm{cal}) = \sqrt{u(\mathrm{abs_{cal}})^2 + \left(\frac{u(\mathrm{stab})}{\sqrt{3}}\right)^2} \left[\%\right], \tag{6}$$

where $u(\mathrm{cal})$ is the radiometric calibration uncertainty for the instruments, $u(\mathrm{abs_{cal}})$ is the uncertainty from the laboratory based absolute radiometric calibration.

The 1 % temporal stability assumption was evaluated by comparing the multispectral instruments in use here with the hyperspectral instruments also deployed on the BOUSSOLE buoy. An Unbiased Percent Difference (UPD) was calculated for all instrument pairs (i.e., multi- vs. hyperspectral Lu, Ed and Es sensors) for a period of three months. The slope of the UPD vs. time relationship gave us a daily relative sensor drift, which, when acumulated over the period under study ended up with a 0.75 % drift.

b. Cosine response

Radiometers measuring plane irradiance, such as the one measuring E_s on top of the BOUSSOLE buoy, are equipped with planar diffusers that collect radiances from all directions of a hemisphere. Ideally the response of the radiometer is proportional to the cosine of the incident angle, having then what is referred to as a perfect cosine response. Instruments always depart from this theoretical behavior, however, and this departure has to be quantified. It is generally below 3 % for incidence angles $< 60^\circ$ and reaches 10 % or more for angles $> 60^\circ$ (Satlantic Inc; personal communication; Multichannel Visible Detector System update Guide MVDS s/n 062). Ideally this departure would be characterized for each instrument, so that a correction for that effect can be applied, and then only a residual uncertainty in that correction would be propagated (Zibordi and Bulgarelli 2007). Such instrument-specific corrections were not available. Cosine response

tests were nevertheless performed occasionally to check if the instruments met these requirements, showing results within the above specifications (actually often better).

Total downward irradiance is made of the direct sun irradiance plus the diffuse sky irradiance. Both components are not affected the same way by a non-perfect cosine response. For the direct irradiance the cosine response is related to the incident angle (in this case the sun zenith angle) and is characterized for each possible value. For the diffuse part the cosine response for all angles is integrated over the whole hemisphere. If we assume an isotropic sky radiance distribution, it is calculated according to:

$$k_{cos_{\mathrm{h}}} = \int_0^{\pi/2} k_{cos}(\theta) sin(2\theta) d\theta \ , \tag{7}$$

where $k_{cos_{\mathrm{h}}}$ is the integrated cosine response over the full hemisphere while $k_{cos}(\theta)$ is a cosine response for a given illumination angle. Actual clear-sky radiance distributions are not isotropic and normally show larger radiances for large angles (e.g., Zibordi and Voss (1989)). The $sin(2\theta)$ factor in Eq. 7 would however minimize their contribution to $k_{cos_{\mathrm{h}}}$. The diffuse component of the downward irradiance for clear skies is about 30 % only, further reducing the impact of $k_{cos_{\mathrm{h}}}$ on the R_{rs} uncertainty evaluation. A thorough evaluation of this effect would nevertheless be timely and would be consider in the succeeding version of the uncertainty evaluation.

The cosine diffuser response or its departure from a perfect cosine response is an example of a systematic error (bias). Because we do not have enough information on the actual cosine response of all our instruments, their possible deviations from an ideal response are not corrected. Therefore we treat this as an uncertainty component. Although not normally recommended (GUM; note 6.3.1), doing so can be justified when the bias is small. Here we treat the residual bias (the signed sum of the individual biases) as an uncertainty component added to other uncertainty components.

We used $k_{cos}(\theta)$ values of 2 % for angles $< 20°$, 3 % for angles $> 20°$ and $< 60°$, 5 % for angles

from 60° to 70°, and 10 % for angles > 70°. The corresponding k_{cos_h} is 3.5 %. These are biases rather than uncertainties, however, which are not corrected so that they are inserted into the model as uncertainty contributors. The PDF for the $k_{cos}(\theta)$ has a rectangular distribution with the upper limit of [1 plus the bias value] (relevant to a given angle cosine response) and the lower limit of [1 minus the bias value]. For example for SZA < 20° the distribution limits would be [0.98, 1.02] and for SZA = 60° [0.95, 1.05]. A similar approach is chosen for k_{cos_h}, where the lower limit is always 0.965 and the upper limit is 1.035.

c. Temperature dependence

The temperature dependence for the dark readings was tested at the NPL facility for a maximum temperature range that is expected at the BOUSSOLE site and varies from 5°C to 30°C (air temperature outside the E_s sensor). Measurements were taken at four separate temperatures (2°C, 12°C, 22°C, and 32°C) and each of these was repeated twice. The change in the dark signal was less than 0.05 % for the entire measured temperature range. The thermal stability of the dark readings ensures that the night measurements can be used for correction of the measurements taken during the day, in particular with maximum diurnal changes in water temperature of about 2°C at 9 m.

The thermal stability of light readings was checked on the E_s sensor data recorded on site. The check is done using the ratio of measured E_s sensor (in cloud free conditions) to the clear-sky modeled values (Gregg and Carder 1990) and the correlation of this ratio with the temperature during the measurement. The correlations were found insignificant for temperature ranging from 19°C-26°C (from -0.12 for 412 nm to -0.09 for 670 nm; otherwise below -0.04), and therefore not accounted for in the current uncertainty evaluation.

d. Effects not accounted for

A few instruments attributes and the uncertainty associated to their characterization are not included in the current version of the uncertainty budget. They include the spectral accuracy, the polarization sensitivity, and the immersion factors. This is not because we consider them negligible *a priori* but because we do not necessarily have the information to model them properly. The uncertainties at stake here are small anyway, yet there is definitely room for improvement here in subsequent versions of the uncertainty budget. The spectral response is defined by the interference filters used in the Satlantic OCR-200 series radiometers with spectral bandwidths of 10 nm, and an out-of-band rejection value provided by the manufacturer of 10^{-6}. These filters were initially characterised but are not re-characterized on a regular basis. They are however replaced during manufacturer calibration if the responsivity of that channel changed significantly, minimizing then the risk of substantial spectral errors. The manufacturer does not report the polarization sensitivity ifor each specific instrument. Nevertheless, the same class of radiometers was used during the SIRREX -7 inter-comparison exercise (Hooker et al. 2002), and showed polarization sensitivity in the range of 1.4 %-2.4 %, which can be considered negligible with regards the state of polarization of underwater nadir radiance (Austin 1974).

Class-based immersion factors for in-water radiance sensors are provided by manufacturers from a basic model based on refractive index of water and glass window (Zibordi 2006). Previous studies, for the type of instruments considered here, report a small negative bias between basic and extended sensor modeling, i.e., when a more realistic optical design of the sensors is taken into account (Zibordi 2006). This bias was estimated at -0.4 % with the uncertainty in the measurements at the level of 0.19 %. More recent studies for the MOBY instrument confirmed that uncertainties of an improved model including transmittance and reflectance of the optical components and the

instrument field of view (FOV) do not differ significantly from those of the basic model (0.05 %, $(k = 1)$, Feinholz et al. 2017). Therefore, the uncertainty related to the immersion factor of radiance radiometers is not included in this budget as it is considered of negligible impact.

4. Uncertainties related to data processing

a. Raw signal statistics(data reduction)

It is reminded here that the median of the 360 values of L_{u4}, L_{u9} and E_s obtained during the 1-min acquisition sequences of instruments operating at 6 Hz are taken as representative values for subsequent calculations of derived quantities such as R_{rs}. Using the median is an efficient way to exclude possible outliers. The dispersion around this median is the result of both the instrument inherent noise plus the changing environmental conditions, in particular focusing and defocusing by capillary waves. The instrument inherent noise, expressed as a standard deviation of the mean of the 360 individual measurements taken in laboratory conditions, was quantified below 0.1 % for all spectral channels and therefore is ignored. The standard deviation of the mean of field measurements is used as a measure of changes in the signal caused by environmental changes during the one-minute measurement sequence. Fig. 2(a) shows a typical one-minute series of $E_s(442)$ measurements, showing low-frequency changes due to slight tilt variations during the measurement sequence. Fig. 2(b) shows a typical one-minute series of $L_{u4}(670)$ measurements, showing high-frequency changes due to wave focusing. Fig. 2(c) shows the distribution of the same 360 values, with indication of the mean and median values. They are both represented as black vertical lines, however nearly superimposed because the distribution is quasi Gaussian. The PDF of the instrument signal will therefore be represented by a normal distribution with a mean equal to the median value of one-minute readings and a standard deviation equal to the standard deviation of

the mean of the same signal series. Thus, the actual spread in the instrument readings, which depends mostly on the environmental conditions during the measurement sequence, is included and carried into the uncertainty estimate for each measurement. The standard deviation of the mean is a representative estimate of uncertainty for random and uncorrelated signals. To ensure that the readings in one-minute acquisitions are not correlated, the Allan deviation test (Allan 1966) was performed, which consisted in computing the standard deviation of sub-samples (clusters) of various size of the 360 measurements. Fig. 3 shows a standard deviation decreasing when the number of samples in each cluster increases, which confirms that measurements are not correlated. The only exception is for the second cluster for which the Allan deviation is higher than for the first sampling interval. This might be caused by matching the sampling rate with the wave-focusing period, thus generating correlation.

b. Tilt-induced uncertainty for depth measurement

By design the BOUSSOLE buoy stands vertical when no force are applied to it other than the balance between gravity and Archimedes buoyancy (upthrust). A pressure sensor nominally installed at a depth close to 9 m provides the buoy level with respect to the air-sea interface. The depth offset of each radiometer with respect to this pressure sensor is measured before deployment, so that the actual measurement depths of L_{u4} and L_{u9} are known. These depths change as soon as the buoy inclines under the effect of currents or oscillates when waves pass through. Geometry calculations using the measured 2-axis tilt allow the actual depth of each sensor to be determined. The uncertainty in these calculations depends on the inherent accuracy of the pressure and tilt sensors, on the accuracy of the measurements of the depth offsets, and on wave height and frequency. The Seabid 37-SI pressure sensor accuracy is stated by the manufacturer as 0.1 % and the stability 0.05 %. The combined uncertainty of those two gives a value of 0.11 %. We assume an uncertainty

of 5 mm for the depth offset measurements, with a rectangular PDF. A specific MC model was run to estimate uncertainty on the instruments depth calculations. Fig. 4 presents histograms of the measurements uncertainty for the lower and upper arms, for a selection of data with tilt values lower than 10 degrees and for which the depth recorded by the pressure sensor nominally at 9 m is not lower than 11 m (which means the buoy is not lowered by more than 2 meters as compared to its nominal position). Most uncertainty values are around 2 cm for measurements from the deeper arm, increasing to 2.6 cm - 2.7 cm for the shallower arm. Higher uncertainties for the instrument located closer to the surface are due to the longer arm length, making the depth change for a given tilt, hence the uncertainty on this depth change, larger than the depth change of the deeper radiometer. The output of this model is integrated to the general BOUSSOLE uncertainty MC model, so that each measurement has an associated depth uncertainty PDF that accounts for actual environmental conditions.

c. Tilt-induced uncertainty for the radiometric measurements

Another consequence of the buoy tilt is that upwelling radiances are no longer measured exactly at nadir, and the above-surface downward irradiance no longer corresponds to the irradiance impinging on a horizontal plane. The corresponding uncertainty for upwelling radiance measurements is therefore related again to the uncertainty in the tilt measurement, and to changes of the upwelling radiance as a function of the viewing angle. These changes are described by the bidirectional reflectance distribution function (BRDF). This part of the uncertainty budget has not been assessed here. It could be evaluated later on, for instance through using existing models of the BRDF as a function of the chlorophyll concentration (e.g., Morel et al. 2002). A correction is however applied to the direct component of the E_s measurement. This component is determined theoretically for clear-sky conditions through the Gregg and Carder (1990) model. The correction

of the direct component uses the ratio of the cosine of the sun zenith angle to the cosine of the actual incident angle on the non-level sensor. This correction requires knowledge of the 2-axis tilt values, the sun zenith angle and the sun azimuth, because a given absolute tilt value does not have the same impact whether the buoy is tilted towards the sun or away from it. The uncertainty of this tilt correction was estimated by running the calculation using normal PDFs of all input components. The mean is equal to the median value of one-minute acquisitions and the standard deviation is the standard deviation of the mean combined with an additional uncertainty related to the sensor accuracy. This accuracy was stated by the manufacturer as 0.5° for the azimuth (heading sensor) and due to the lack of such information for the tilt, the same value is used. Results are presented in Fig. 5(a), for the same data set as in Fig. 4. Most uncertainty values are lower than 1 %. These uncertainties of the tilt correction increases with the sun zenith angle, as shown in Fig. 5(b). The outputs from this model are integrated to the main MC model, thus each observation will have an uncertainty in the tilt correction based on the actual measurement conditions during that acquisition.

d. Shading effects

Self-shading of instruments cannot be avoided and, although the BOUSSOLE buoy has been designed to minimize perturbations of the underwater light field by the buoy structure, it cannot fully eliminate such effects either. The combined self-shading of instruments and instrument shading and reflections of the BOUSSOLE buoy was modeled with the SimulO three-dimensional (3D) backward Monte Carlo Code (Leymarie et al. 2010). This model takes into account the 3D structure of the buoy and instruments, and sets the sun position (zenith and azimuth angles, with 5° steps) with respect to it. Spectral optical properties are modeled as a function of the chlorophyll concentration (0.1, 0.5, 1.0 and 5.0mg m^{-3}). Running the model with the same environmental

conditions in absence of the buoy structure and instrument body allows generating a shading correction coefficients look-up table (LUT). An example of shading correction is presented in Fig. 6. The shading correction coefficient is then interpolated from LUTs and applied as a multiplicative factor to each measurement depth (z_4 and z_9) and wavelength separately. A 5 % threshold for the shading correction coefficient was used as rejection criterion in the quality control procedure. The uncertainty in shading corrections is estimated from a model validation exercise that compared the outputs from the SimlO to the results of Piskozub (2004), showing differences of 2 %. Although this value cannot fully represent the uncertainty in the shading correction, it is used as an indication until a better solution is found. The shading correction is derived for each spectral band at two depths for every measurement in the data series. In the MC model, that shading correction value is propagated in the form of a rectangular distribution, where the lower and upper limits are defined as the actual shading correction coefficient value ± 2 %. The 683 nm band is the only exception where, due to very low number of photons the SimlO cannot provide a solution. In the processing a shading correction coefficient from the closest modeled band (670 nm) is used with an increased uncertainty value of ± 3 %.

e. Extrapolation to the surface

The L_u measurements from nominally 4 and 9 meters, L_u4 and L_u9, are used to calculate K_{L_u}, and L_u4 is then extrapolated to just below the surface to get $L_\mathrm{u}(0^-)$ using Eq. 3. Diffuse attenuation coefficients in the upper layers (first optical depth) are not constant with depth, however. Therefore, the K_{L_u} determined from L_u4 and L_u9 might not always provide accurate extrapolation from 4 m to the 0^- level. This is particularly true for wavelengths above 600 nm. A correction to Eq. 3 was therefore introduced in (Antoine et al. 2008a, (Appendix A), which is based on radiative transfer computations including multiple scattering and the Raman contribution (using

Hydrolight, Mobley 1994). These computations were run for chlorophyll concentrations and solar zenith angles with the same resolution of 3D MC shading model, and results are used to build an extrapolation correction coefficient LUT. Inputs to the correction are the sun zenith angle and the chlorophyll concentration, which is used as index of the optical properties (see Appendix B in Antoine et al. 2008a, for determination of this concentration). We assume here no uncertainty due to the calculation of the sun zenith angle. The sensitivity of the correction to the chlorophyll concentration was tested for chlorophyll concentrations from 0.1 to 0.6 mg m^{-3}, to which a ± 20 % error was assigned. Average results over sun zenith angles in the 20-60 degrees range are presented in Fig. 7. They show a negligible impact in the blue-green spectral range and errors of 2-3 % for red channels. Values of 0.5 % are therefore used for the overall uncertainty on the extrapolation correction, for wavelengths below 600 nm. For the red bands the value strongly depends on the chlorophyll concentration, the effects of SZA are minimal. Thus, this uncertainty for wavelengths above 600 nm and chlorophyll concentration below 0.25 mg m^{-3} is estimated as 2 %, and set at 3 % for higher concentrations but not exceeding 0.6 mg m^{-3} (consistently with the data set considered here).

f. Transmission across the air-sea interface

Although the commonly agreed value of 0.543 for the $(1-\rho)/n^2$ factor is used in Eq. 2, an uncertainty has to be assigned here as well. The main source of information about this number and its calculation are from (Austin 1974) and (Austin and Halikas 1976). More recently (Wei et al. 2015) tried to confirm the theoretical value with *in-situ* measurements and found in principal good agreements between the two, but the constant value used there was 0.54 and the level of its accuracy of 10 % is far lower than the SVC needs. (Voss et al. 2017b) also quantified the spectral dependency of this factor. The relative uncertainty of the transmission factor using the traditional

GUM approach is given by:

$$\left(\frac{u(C_{\rho n})}{C_{\rho n}}\right)^2 = \left(\frac{u(\rho)}{(1-\rho)}\right)^2 + \left(\frac{2u(n)}{n}\right)^2, \tag{8}$$

where $\frac{u(\rho)}{(1-\rho)}$ is a relative uncertainty in the nominator related purely to the uncertainty in the Fresnel reflection coefficient, and $\frac{2u(n)}{(n)}$ is a relative uncertainty in the denominator of the same equation related to refractive index of seawater, n. Because n is squared, the sensitivity coefficient assigned to its uncertainty is 2, which means that the refractive index uncertainty contributes more to the transmission factor uncertainty than that of ρ.

The index of refraction of seawater depends on water salinity, temperature, pressure, and varies spectrally. The tables from Austin and Halikas (1976) were used to verify the range of the n changes. Table 2 presents values for the first three variables recorded during one BOUSSOLE deployment (consistently with the data set considered here). There is very little change in the salinity and atmospheric pressure for the data records in the current data set, thus these two factors are not considered further. The temperature range is around 6°C, according to the data from the (Austin and Halikas 1976, Table 4-2) the difference in n at 20°C and 25°C is 0.04 %, thus very small and considered as negligible. This value increases to 0.15 % for 10°C to 30°C temperature range, which is representative for the entire BOUSSOLE data set. The change in the refractive index between the 412 nm and 683 nm was calculated using the data from (Austin and Halikas 1976, Table 4-2) for a salinity of 34.99 psu and an atmospheric pressure of 0 kg/cm^2. A second order polynomial was fitted to the data from the report to estimate the refractive index values. The refractive index estimated range is between 1.3362 and 1.34894 for wavelengths from 683 nm to 412 nm, and is 1.34199 for the 510 nm band that provides an exact 0.543 constant value. These spectral changes in n are the major contributors to the overall uncertainty and for the two border wavelengths this effect on $u(C_{\rho n})$, calculated using only the second component of the right-hand

side of Eq. 8, is 0.89 %, decreasing to 0.53 % for the wavelengths in between. Major variables affecting the Fresnel reflection coefficient are wind speed and viewing angle. Data considered here were collected with winds speeds below 10 m/s^2 and for a viewing angle up to 10°. This means that the ρ value could vary from 0.0211 to 0.0218 (Austin 1974). Uncertainty in $C_{\rho n}$ due to ρ, calculated using only the first component of the right-hand site of Eq. 8, is 0.042 %, that when combined with the second part of the same equation does not change the final result. Thus, an uncertainty of 0.89 % is assigned to 412 nm and red wavelengths, whereas a value of 0.53 % is used for the remaining spectral bands. Consequently the PDF for this component has a normal distribution with a mean value 0.543 and a standard deviation varying with wavelength as stated above. This is actually a bias not an uncertainty and according to the GUM this bias should be corrected and then any residual uncertainty related to that correction can be propagated. This is not done in this case and the present uncertainty budget is calculated for the existing processing and currently there is no correction for that.

g. Solar irradiance modeling

When evaluating the uncertainty due to imperfect cosine response of the E_s sensor, the ratio of diffuse to direct sunlight was used. This E_s ratio is derived from the (Gregg and Carder 1990) spectral solar irradiance model. The model needs wind speed, relative humidity and atmospheric pressure as inputs, which were taken from the meteorological buoy deployed in the vicinity of BOUSSOLE. It also needs the total ozone content, which is calculated daily based on the geographic position and the Julian day, and the precipitable water content, set to 2 cm. It is reported by (Gregg and Carder 1990) that their model agrees within 6.2 % root mean square (RMS) value with spectral irradiance measurements for the wavelength range from 400 nm to 700 nm. Again, the RMS value is not here a real uncertainty of the model, but this is a good indication of the

model capabilities. Actual uncertainty in the model might be lower as the RMS value includes some of the uncertainties that are associated with the spectral irradiance measurements used for its assessment. Nevertheless, we assign a rectangular PDF to the direct to total irradiance fraction f_{dir}, where the upper limit is defined as given E_{s} ratio plus 6.2 % of that value and lower limit as given E_{s} ratio minus 6.2 % of that value.

5. Combining uncertainties

a. The final measurement equation including correction factors

Eq. 5 can now be expanded by including all factors that come into play in the data processing and for which uncertainties have been devised in the previous sections, as follows:

$$R_{\mathrm{rs}} = \frac{L_{\mathrm{u4}} k_{\mathrm{cal}} f_{s_4} exp\left(- \frac{ln(L_{\mathrm{u9}} k_{\mathrm{cal}} f_{s_9} / L_{\mathrm{u4}} k_{\mathrm{cal}} f_{s_4})}{z_9 - z_4} z_4 \right) f_h \left(\frac{1-\rho}{n^2} \right)}{E_{\mathrm{s}} k_{\mathrm{cal}} k_{cos} f_{tilt} f_{dir} + (1 - f_{dir}) E_{\mathrm{s}} k_{\mathrm{cal}} k_{cos_{\mathrm{h}}}} , \tag{9}$$

where L_{u4}, L_{u9} and E_{s} are median values of 1-minute measurement sequences (in physical units) minus dark readings, k_{cal} represents the uncertainty in absolute radiometric calibration, k_{cos} and $k_{cos_{\mathrm{h}}}$ are uncertainties due to the cosine response of the irradiance sensor diffuser affecting the direct sun irradiance and the total diffuse integrated over the hemisphere, f_{s_4} and f_{s_9} are shading corrections for radiance applied at the depth of 4 m and 9 m, f_h is the Hydrolight-based extrapolation correction, f_{tilt} is the tilt correction on E_{s} and f_{dir} is the fraction of direct to total solar irradiance. All k factors have a mean of their PDFs equal to 1 and PDFs limits defined by a given uncertainty value.

Table 4 summarizes the main sources of uncertainty and parameters from the measurement equation Eq. 9 affected by them. Correlation between them can be clearly seen as often more than one parameter is related to a single uncertainty contributor.

b. The Monte Carlo Method

To evaluate the uncertainty related to the derivation of R_{rs} through Eq. 9, the GUM (JCGM100 2008) methodology is followed. A quadratic sum of the various individual uncertainties is often used to derive a relevant overall uncertainty, which is indeed defined in the GUM as simplest example to combine uncertainty of uncorrelated inputs. This is, however, clearly not adapted to Eq. 9. Here, the Monte Carlo Method (MCM) is used, which is known as Supplement 1 to GUM (JCGM101 2008). The MCM uses the PDF of each input component instead of its uncertainty value. The measurement model, here Eq. 9, is run a large number of times (here typically 10^5) for a given [L_{u4}, L_{u9}, E_s] triplet, each run including values for the various factors randomly drawn from the PDFs. The many Rrs values generated this way have their own PDF, from which the best estimate and its associated standard uncertainty $(k = 1)$ value can be derived. When the output PDF is close to Gaussian, the mean and standard deviation are suitable to derive the representative value and its uncertainty. With this MCM, an uncertainty is produced for each R_{rs} value derived from a single [L_{u4}, L_{u9}, E_s] triplet. This uncertainty takes into account the environmental conditions that were present during its acquisition. From this, an overall uncertainty budget can be derived for any data set that would be used for a given purpose. In the following section, such a budget is derived for a data set that would be suitable for system vicarious calibration of an ocean color sensor, in which case uncertainties have to be kept minima.

c. Selecting a demonstration data set

In order to illustrate the application of the MCM to determining an uncertainty budget for a given dataset, we have selected a subset of BOUSSOLE data following criteria (Table 4) that qualify them *a priori* for being used for satellite ocean color SVC. These data accordingly have to be of the lowest possible uncertainty. The condition on stability of the 1-minute readings is

to avoid situations with rapidly changing above-water (clouds, birds) irradiances. The clear-sky test compares the measured downward irradiance to the theoretical value derived from the Gregg and Carder (1990) model, and only keeps data for which the difference is within 10 %. The tilt and depth conditions eliminate measurements taken with high wind speeds (typically greater than 10 m/s), which are unwanted because of whitecaps. Keeping data only for sun zenith angles less than 75 degrees eliminates data collected in the early morning or late afternoon, or at midday in winter. Data for which the shading correction is larger than 5 % are not considered. Finally, data suspected of being contaminated by bio-fouling are not included here, as well as data showing inter calibration issues (can be seen for some deployments where the whole dataset tends not to agree with that from other years). The possible presence of biofouling is determined by visual screening of the time series of the following ratios of radiometric quantities: L_{u9}/L_{u4}, L_{u4}/E_s and L_{u9}/E_s. This is performed at individual wavelengths because biofouling might affect differently each radiometer channels (by design: one collector per wavelength). In particular the presence of step changes in these ratios after divers cleaning on the optical surfaces is used as an indicator of biofouling contamination.

We have applied these criteria to data from one summer deployment of BOUSSOLE, from June to August 2008, which resulted in 1090 individual observations.With the method proposed here, there is no need to claim that all of these 1090 observations are necessarily usable for SVC. The criteria we used to select them only make them *a priori* usable for SVC. Their use for SVC is however eventually and only determined by how small the individual uncertainty attached to each of them is. We could have used any other equivalent BOUSSOLE deployment data subset for this demonstration. The only difference would have been on the final proportion of measurements having an uncertainty below a predefined threshold within the set of *a priori* selected measurements.

d. Uncertainty budget for the SVC data set

The results are presented at different processing steps to show the uncertainty value evolution from the measurement at a single depth through to calculation of the attenuation coefficient from two radiances at different depths and finally to the final product, R_{rs}. The uncertainties of $L_{\mathrm{u}4}$ are presented in Fig. 8 for four of the seven spectral channels. They include the uncertainty from instrument calibration, from the signal statistics and from the shading correction k_{cal} and f_{s_4}. These values are driven by the instrument calibration uncertainty, the signal statistics (how much the signal fluctuates during the 1-min sequences), and the uncertainty of the shading correction. The two latter are higher and dominate the uncertainties for red bands ($\lambda = 683$ nm in Fig. 8), which also have significantly lower signal to noise ratios than the shorter wavelength channels, for which the environment effects are not noticeable. The uncertainty is higher for $\lambda = 510$ nm than for the blue bands, because of the non-uniformity of the calibration source (the FEL lamp for irradiance and then the reflectance panel illuminated by that lamp for radiance; see Table 1 for radiometric calibration uncertainty values). Outliers with larger uncertainty values indicate imperfect data screening.

The total uncertainties of the attenuation coefficient, $K_{L_{\mathrm{u}}}$, include uncertainties of radiometric measurements at 4 and 9 meters, their correlation (see APPENDIX for more details about correlation) and uncertainties in depth measurements. This uncertainty is presented in absolute values m^{-1} in Fig. 9. The highest uncertainties in the attenuation coefficient are observed for the 683 nm band. The remaining spectral channels have similar $0.003\ \mathrm{m}^{-1}$ uncertainty. Contrary to what was observed for $L_{\mathrm{u}4}$, the uncertainty for 510 nm is at the same level as the other blue/green spectral bands. The calibration uncertainty that pulled up this value for $L_{\mathrm{u}4}$ is no longer as dominate as the calibration uncertainty for the radiometers at two depths are strongly correlated. To account for

that correlation the same draw from the k_{cal} PDF is used when deriving L_{u4} and L_{u9} and combining them to get K_{L_u}.

The next processing step is the extrapolation of L_{u4} to the 0^- level, so as to get $L_u(0^-)$. This is where the uncertainty in the Hydrolight-based correction comes into play. Results are shown in Fig 10. The uncertainty in $L_u(0^-)$ depends on the actual depth where L_{u4} was measured. Indeed, the shorter the extrapolation distance, the more certain the value of $L_u(0^-)$. If the traditional GUM approach using the Law of Propagation of Uncertainty was used, the relative uncertainty in $L_u(0^-)$ would be expressed as:

$$\frac{u^2(L_u(0^-))}{L_u(0^-)^2} = \frac{u^2(L_{u4})}{L_{u4}^2} + z^2 u^2(K_{L_u}) + K_{L_u}^2 u^2(z) \ . \tag{10}$$

Thus, the depth of the instruments has a role of sensitivity coefficient for the attenuation coefficients uncertainty. This effect is presented in Fig. 11, where the correlation between the actual depth of the radiometer and the uncertainty in $L_u(0^-)$ is clearly visible.

The uncertainty in L_w is displayed in Fig 12, where the uncertainty on the transmission factor across the sea-air interface is now included. This uncertainty is low overall, yet slightly higher for the shortest and longest wavelengths.

The uncertainty of E_s is affected by the tilt of the buoy and the sun zenith angle, which determines proportions of diffuse and direct irradiance (Fig. 13). The decrease of uncertainty with increasing sun zenith angle up to values of 60 degrees corresponds to the decreasing proportion of direct light. The step change at a sun zenith angle of 60° is caused by a step change in the uncertainty of the response of the cosine diffuser to direct light (as provided by the manufacturer). The time series of the uncertainty in the final product, R_{rs}, is presented in Fig. 14(a). The same data are plotted as a function of SZA on Fig. 14(b). The two red channels exhibit the highest uncertainty values because they are more significantly driven by the environmental conditions, as

well as by the shading and the extrapolation corrections. For these wavelengths > 600 nm the instrument-related uncertainties are lower and the absolute radiometric calibration sources have lower uncertainties. The blue channels have higher instrumental-related uncertainties. The environment does affect them less than the red channels, however, thus their overall uncertainty is below 4 %.

Summary values of these uncertainties are shown in Table 5, for each radiometric quantity and the final R_{rs}, and for each wavelength. The values in Table 5 are calculated as the highest density probability from all uncertainties calculated for each data point. Example histograms of uncertainties values obtained from all data products form the study data set for selected spectral bands are shown in Fig. 15. They clearly show the most likely reachable uncertainty (mode of the histograms). They also show that lower and higher values can be observed depending on the actual conditions at the site. Key here is that these uncertainties are available for every individual measurement, which then allows selecting data sets using any threshold on uncertainties. This threshold must be low for SVC of satellite ocean color observations, might be somewhat relaxed for validation of OCR-derived R_{rs}, and will depend on the question at hand when it comes to analyzing data for science purposes. The model results were found to be stable within 0.1 % by comparing the summary output values from multiple runs of the same simulation (using 10^5 individual runs each time).

6. Conclusions

A method has been presented that allows providing an uncertainty estimate when deriving the remote-sensing reflectance, R_{rs}, from measurements of underwater upwelling nadir radiances at two depths combined with the above-water plane irradiance. This uncertainty is derived from combining individual uncertainty sources (values) through a Monte Carlo Method (MCM). A pre-

requisite is that these individual sources of uncertainty have been identified and quantified. In this particular case, their probability distribution functions have to be either determined for type A uncertainties or specified for type B uncertainties. Contrary to using a quadratic sum of individual uncertainty components, the MCM allows addressing correlations between some of the input components. This can be done either explicitly (e.g., by selective sampling of the PDFs of each input component) or implicitly through the way these input components are combined through the measurement equation (here Eq. 9). As a practical example, we applied the method to a subset of data from the BOUSSOLE time series. The goals are to illustrate the capability of the method and to provide a preliminary uncertainty budget for the BOUSSOLE radiometric measurements, when these measurements respect criteria making them *a priori* usable for satellite ocean colour SVC (such as a low buoy tilt). This method has the advantage of evaluating uncertainty for each observation instead of providing one generic value for an entire dataset or project. These uncertainty values include the instrument-related uncertainties, the processing-related uncertainties, as well as the effect of changes in environmental conditions during the measurements. It is then up to any data user to decide whether a particular measurement with its associated uncertainty is suitable for further use or not. Any field site that delivers yearlong records of radiometry measurements taken throughout each and every day will end up with delivering data whose uncertainties are going to be highly variable. When taken in ideal conditions, e.g., low chlorophyll concentration, low wind speed, clear sky and high solar zenith angle, the measurement uncertainty will be low (assuming instruments are well calibrated and characterized). When those conditions are not met, higher uncertainties will occur. That is why defining a typical uncertainty for a given site does not make sense if the typical range of environment conditions is not specified. For example, an average uncertainty might be delivered for all BOUSSOLE measurements taken within an hour of solar noon and when the sky is clear. Another uncertainty budget would be obtained if all measurements form

dawn to dusk are considered. And still another number if cloudier conditions would be included. That is where the individual uncertainties will reveal powerful when the full time series will have been characterised: when ocean colour SVC is at stake, we can filter out any measurement whose uncertainty is larger than a given threshold, so that we provide a qualified SVC data set. The threshold could be larger if the data were to be used for another purpose, ending up with more data being usable (could be, e.g., for geophysical products validation or for bio-optics research). This method also allows better understanding of the respective importance of various uncertainty sources in driving the final uncertainty either on a given measurement or for a given ensemble of measurements. This capability provides a way to improve either the experimental set up or the data processing chain or both. For example, the uncertainty on the air-water transmission constant has been shown to have a significant impact, and then could be made wavelength-dependent in future versions of the data processing. Similarly, the observed correlation between the depth of the shallowest instrument and $L_u(0^-)$ advocates for moving the shallowest depth of measurement closer to the surface. Stronger wave focusing would however affect the measurement, and then increasing uncertainty on that side. Therefore, the overall uncertainty has to be considered globally for the whole system, inasmuch as individual components separately affect different aspects of the measurements. This example shows that this framework in not only helpful to provide users with fit-for-purpose criteria but also to better understand the critical components of the system and ultimately improve it. The uncertainty in E_s is affected by the non-perfect cosine response of the diffuser, and therefore is related to the sun zenith angle. Recent recommendations (Mazeran et al. 2017) are to derive R_{rs} using a modeled value of E_s instead of the measured one, when R_{rs} is to be used for SVC purposes. The logic is that using the same model as used by the satellite data processing chain, rather than the *in-situ* measurement, would improve consistency and accuracy

of the SVC. If going that way, trying to reduce uncertainties on the E_s measurement would be of less importance in the context of SVC.

The R_{rs} relative uncertainty for the red channels in clear waters such those at BOUSSOLE will always be larger due to low signal levels. As the final quantity is close to zero, the relative uncertainty is high. For example, a typical value of L_w at 440 nm is 0.8458 μWcm^{2}nm^{-1}sr^{-1} and relative uncertainty 3.11 % (and 0.0226 in radiance units). At 680 nm, L_w is 0.0187 μWcm^{2}nm^{-1}sr^{-1} with relative uncertainty 4.90 % (and 0.0008 in radiance units).

Further work will apply the same methodological framework to hyperspectral radiometers that are also in operation on the BOUSSOLE buoy. These radiometers will have more uncertainty components related to their characteristics and differences in their operation mode, such as varying integration times and more dark readings interspersed among light measurements. A detailed and comprehensive uncertainty evaluation will then become reachable.

Acknowledgments. BOUSSOLE is funded by the European Space Agency (ESA), the Centre National d'Etudes Spatiales (CNES), the Centre National de la Recherche Scientifique (CNRS), the Institut National des Sciences de l'Univers (INSU), the Sorbonne Université (SU), and the Institut de la Mer de Villefranche (IMEV). The authors acknowledge Météo-France for supplying data from the Azur meteorological buoy, and the HyMeX database teams (ESPRI/IPSL and SEDOO/Observatoire Midi-Pyrénées) for their help in accessing the data. Edouard Leymarie is kindly acknowledged for running SimulO computations. This research was partly supported by the EURAMET EMRP ENV-53 project. The EMRP is jointly funded by the EMRP participating countries within EURAMET and the European Union.

APPENDIX

Error correlation

Firstly, we remind here the basic definitions of an error and measurement uncertainty as they are stated in the GUM and how there they are applied in the MCM approach.

An error is *the difference between a measurement value and a reference value*. An uncertainty is *a parameter characterizing the dispersion of the values being attributed to a quantity, based on information used* . For the MCM model the reference values are the means of PDFs, and the uncertainty is the standard deviation of the PDF, if that PDF has a Gaussian shape or is close-enough to a Gaussian shape. The errors are the differences from the reference value used in the MCM processing and individual draws from the PDF assigned to this value. When we refer to correlation, it is important to note that only errors of a given quantity can be correlated, thus we talk about error (not uncertainty) correlations. The error correlations between input quantities of the measurement equation have been assessed for two wavelengths (412 nm and 683 nm). Results are presented on Figs. A1 and A2. They show error correlations between the input quantities used to derive L_{w} (see Figure legend). The 1000 error values for each quantity are extracted from the MCM calculations for one measurement from the database. The diagonal of the figure shows the PDFs of each quantity. The lower triangle shows the scatter plot between two components, the upper triangle the correlation value as a number and its significance level, p-value. The size of the displayed correlation coefficients depend on theirs values and significance level, thus low values are made explicitly smaller on the plot. The latter is expressed as asterisks, where the three stars are assigned to the significant p-value with a numerical value in the range of (0, 0.001). As expected significant correlation between the errors of $L_{\mathrm{u}4}$ and $L_{\mathrm{u}9}$ can be seen for both wavelengths ($r = 0.76$ for $\lambda = 412$ m, $r = 0.59$ for $\lambda = 683$ m). This is caused by the absolute calibration (instruments were calibrated in the same laboratory against the same absolute radiometric standards), whose uncertainty is the main contributor to uncertainty in Lu measurements. The reason for the lower correlation at 683 nm is related to the random uncertainty components related to the signal noise,

which is larger for the red wavelengths (see Fig. 8). and, although environmental conditions are common to the measurements at 4 and 9 meters they affect them differently. For example, wave-focusing effects at 4 m and 9 m are different and the random instrument noise has different levels depending on the depth.

The errors in the measurement of depth are not correlated with any of the other errors presented here. The shading correction errors of the upper arm show a negative correlation with the upwelling radiance measurement errors at this depth, and to all other components where this measurement is used, thus to errors of K_{L_u} and L_w. The negative relationship is expected as the errors are presented in the absolute form. Thus, higher L_u values are less affected by the shading correction error. The shading correction errors are drawn from the rectangular PDF defined as 2 % of the shading correction value. The error of the Hydrolight correction is uncorrelated with any of the input parameters but presents some correlation with the errors in L_w. This is relatively low for the blue channel ($r = -0.21$) and more significant for the red one ($r = -0.63$). The above explanation for the negative correlation for shading correction applies to errors in the Hydrolight correction as well. Although, the error correlation is usually presented for the input components, in this analysis we assume the L_w as the output quantity. This is an example of additional information that can be seen on the scatter plots presented on Fig. A1 and A2. The bottom row of the scatter plots shows how the output quantity errors are correlated with the input errors. The last column holds error correlation values of the input components and L_w. This can be interpreted as how much weight a given component has on the L_w uncertainty. Thus, the uncertainty on the water leaving radiance is mainly driven by the uncertainty in the L_u measurements at the shallowest depth, because their errors are highly correlated: the value in the top right corner of the Fig. A1 and A2 is the highest in this column. Then we start to see differences between the 412 nm and 683 nm spectral bands. Clearly for the blue wavelength the measurement uncertainty from 9 m still contribute to the result

with the error correlation value of 0.47 in the second row on the last column in Fig. A1. Whereas for the red channel the equivalent number is only 0.18.

References

Allan, D. W., 1966: Statistics of atomic frequency standards. *Proceedings of the IEEE*, **54 (2)**, 221–230, doi:10.1109/PROC.1966.4634.

Antoine, D., F. d'Ortenzio, S. B. Hooker, G. Becu, B. Gentili, D. Tailliez, and A. J. Scott, 2008b: Assessment of uncertainty in the ocean reflectance determined by three satellite ocean color sensors (MERIS, SeaWiFS and MODIS-A) at an offshore site in the Mediterranean sea (BOUSSOLE project). *JOURNAL OF GEOPHYSICAL RESEARCH-OCEANS*, **113 (C7)**, doi: 10.1029/2007JC004472.

Antoine, D., P. Guevel, J.-F. Deste, G. Becu, F. Louis, A. J. Scott, and P. Bardey, 2008a: The "BOUSSOLE" buoy - A new transparent-to-swell taut mooring dedicated to marine optics: Design, tests, and performance at sea. *JOURNAL OF ATMOSPHERIC AND OCEANIC TECHNOLOGY*, **25 (6)**, 968–989, doi:10.1175/2007JTECHO563.1.

Antoine, D., and Coauthors, 2006: BOUSSOLE: A Joint CNRS-INSU, ESA, CNES, and NASA Ocean Color Calibration and Validation Activity. Tech. rep., Goddard Space Flight Center Greenbelt, Maryland 20771.

Austin, R., and G. Halikas, 1976: The Index of Refraction of Seawater. Scripps Institution of Oceanography AD-A024 800, Naval Supply Center, U.S. DEPARTMENT OF COMMERCE National Technical Information Service, 134 pp.

Austin, R. W., 1974: The remote sensing of spectral radiance from below the ocean surface. *Optical Aspects of Oceanography*, N. G. Jerlov, and E. Steemann-Nielsen, Eds., Elsevier, New York., 317 344.

Brown, S., and Coauthors, 2007: The marine optical buoy (MOBY) radiometric calibration and uncertainty budget for ocean color satellite sensor vicarious calibration. Vol. 6744, 6744 – 6744 – 12, doi:10.1117/12.737400, URL https://doi.org/10.1117/12.737400.

Clark, D. K., H. R. Gordon, K. J. Voss, Y. Ge, W. Broenkow, and C. Trees, 1997: Validation of atmospheric correction over the oceans. *Journal of Geophysical Research: Atmospheres*, **102 (D14)**, 17 209–17 217, doi:10.1029/96JD03345, URL https://agupubs.onlinelibrary.wiley.com/doi/abs/10.1029/96JD03345, https://agupubs.onlinelibrary.wiley.com/doi/pdf/10.1029/96JD03345.

Donlon, C., and Coauthors, 2012: The Global Monitoring for Environment and Security (GMES) Sentinel-3 mission. *Remote Sensing of Environment*, **120**, 37 – 57, doi:https://doi.org/10.1016/j.rse.2011.07.024, URL http://www.sciencedirect.com/science/article/pii/S0034425712000685, the Sentinel Missions - New Opportunities for Science.

Feinholz, M., B. C. Johnson, K. Voss, M. Yarbrough, and S. Flora, 2017: Immersion Coefficient for the Marine Optical Buoy (MOBY) Radiance Collectors. *Journal of research of the National Institute of Standards and Technology*, **122**, doi:10.6028/jres.122.031.

Gordon, H., 1998: In-Orbit Calibration Strategy for Ocean Color Sensors. *Remote Sensing of Environment*, **63 (3)**, 265 – 278, doi:https://doi.org/10.1016/S0034-4257(97)00163-6, URL http://www.sciencedirect.com/science/article/pii/S0034425797001636.

Gordon, H. R., 1997: Atmospheric correction of ocean color imagery in the Earth Observing System era. *Journal of Geophysical Research: Atmospheres*, **102 (D14)**, 17 081–17 106, doi:10.1029/96JD02443, URL https://agupubs.onlinelibrary.wiley.com/doi/abs/10.1029/96JD02443, https://agupubs.onlinelibrary.wiley.com/doi/pdf/10.1029/96JD02443.

Gordon, H. R., and D. J. Castaño, 1987: Coastal Zone Color Scanner atmospheric correction algorithm: multiple scattering effects. *Appl. Opt.*, **26 (11)**, 2111–2122, doi:10.1364/AO.26.002111, URL http://ao.osa.org/abstract.cfm?URI=ao-26-11-2111.

Gordon, H. R., and D. K. Clark, 1981: Clear water radiances for atmospheric correction of coastal zone color scanner imagery. *Appl. Opt.*, **20 (24)**, 4175–4180, doi:10.1364/AO.20.004175, URL http://ao.osa.org/abstract.cfm?URI=ao-20-24-4175.

Gregg, W., and K. Carder, 1990: A Simple Spectral Solar Irradiance Model for Cloudless Maritime Atmospheres. *LIMNOLOGY AND OCEANOGRAPHY*, **35 (8)**, 1657–1675.

Gregg, W. W., and C. S. Rousseaux, 2014: Decadal trends in global pelagic ocean chlorophyll: A new assessment integrating multiple satellites, in situ data, and models. *Journal of Geophysical Research: Oceans*, **119 (9)**, 5921–5933, doi:10.1002/2014JC010158, URL https://agupubs.onlinelibrary.wiley.com/doi/abs/10.1002/2014JC010158, https://agupubs.onlinelibrary.wiley.com/doi/pdf/10.1002/2014JC010158.

Harvey, E. T., S. Kratzer, and P. Philipson, 2015: Satellite-based water quality monitoring for improved spatial and temporal retrieval of chlorophyll-a in coastal waters. *Remote Sensing of Environment,*, **158**, 417–430, doi:10.1016/j.rse.2014.11.017, URL https://app.dimensions.ai/details/publication/pub.1021691894, exported from https://app.dimensions.ai on 2019/03/13.

779 Henson, S. A., J. L. Sarmiento, J. P. Dunne, L. Bopp, I. Lima, S. C. Doney, J. John, and
780 C. Beaulieu, 2010: Detection of anthropogenic climate change in satellite records of ocean
781 chlorophyll and productivity. *Biogeosciences*, **7 (2)**, 621–640, doi:10.5194/bg-7-621-2010,
782 URL https://www.biogeosciences.net/7/621/2010/.

783 Hooker, S. B., W. E. Esaias, G. C. Feldman, W. W. Gregg, and C. R. Mc Clain, 1992: An overview
784 of SeaWiFS and ocean colour in Seawifs Technical Report Series. NASA Tech. Memo 104566,
785 NASA Goddard Space Flight Centre.

786 Hooker, S. B., S. McLean, M. Sherman, J.and Small, G. Lazin, G. Zibordi, and J. Brown,
787 2002: The Seventh Seawifs Intercalibration Round-Robin Experiment (SIRREX-7). NASA
788 Tech. Memo 2002-206892, Vol. 17, NASA Goddard SpaceFlight Center, Greenbelt, MD.

789 JCGM100, 2008: Evaluation of measurement data - Guide to the expression of uncertainty in
790 measurement. Guidance document, BIPM.

791 JCGM101, 2008: Evaluation of measurement data - Supplement 1 to the "Guide to the expression
792 of uncertainty in measurement" - Propagation of distributions using a Monte Carlo method.
793 Guidance document, BIPM.

794 Lafaye, M., 2017: Benefit Assessment of the Application of Satellite Earth Observation for So-
795 ciety and Policy: Assessing the Socioeconomic Impacts of the Development of Downstream
796 Space-Based Earth Observation Applications. *Satellite Earth Observations and Their Impact*
797 *on Society and Policy*, M. Onoda, and O. R. Young, Eds., Springer Singapore, 93-103.

798 Leymarie, E., D. Doxaran, and M. Babin, 2010: Uncertainties associated to measurements of
799 inherent optical properties in natural waters. *Appl. Opt.*, **49 (28)**, 5415–5436, doi:10.1364/AO.
800 49.005415, URL http://ao.osa.org/abstract.cfm?URI=ao-49-28-5415.

Mazeran, C., C. Brockmann, K. Ruddick, K. Voss, and F. Zagolski, 2017: Requirements for Copernicus Ocean Colour Vicarious Calibration Infrastructure. Tech. Rep. REF: SOLVO/EUM/16/VCA/D8, EUMETSAT.

Mélin, F., G. Sclep, T. Jackson, and S. Sathyendranath, 2016: Uncertainty estimates of remote sensing reflectance derived from comparison of ocean color satellite data sets. *Remote Sensing of Environment*, **177**, 107 – 124, doi:https://doi.org/10.1016/j.rse.2016.02.014, URL http://www.sciencedirect.com/science/article/pii/S0034425716300426.

Mobley, C. D., 1994: *Light and water: radiative transfer in natural waters*. Academic press.

Morel, A., D. Antoine, and B. Gentili, 2002: Bidirectional reflectance of oceanic waters: accounting for Raman emission and varying particle scattering phase function. *Appl. Opt.*, **41 (30)**, 6289–6306, doi:10.1364/AO.41.006289, URL http://ao.osa.org/abstract.cfm?URI=ao-41-30-6289.

Mueller, J. L., and Coauthors, 2003: Ocean Optics Protocols For Satellite Ocean Color Sensor Validation, Revision 4, Volume v: Special Topics in Ocean Optics Protocols and Appendices. Tech. rep., Goddard Space Flight Center Greenbelt, Maryland 20771.

Piskozub, J., 2004: Effect of 3-D instrument casing shape on the self-shading of in-water upwelling irradiance. *Opt. Express*, **12 (14)**, 3144–3148, doi:10.1364/OPEX.12.003144.

Rast, M., J. L. Bezy, and S. Bruzzi, 1999: The ESA Medium Resolution Imaging Spectrometer MERIS a review of the instrument and its mission. *International Journal of Remote Sensing*, **20 (9)**, 1681–1702, doi:10.1080/014311699212416, URL https://doi.org/10.1080/014311699212416, https://doi.org/10.1080/014311699212416.

Rogers, A., J. L. Blanchard, and P. J. Mumby, 2018: Fisheries productivity under progressive coral reef degradation. *Journal of Applied Ecology*, **55 (3)**, 1041–1049, doi:10.1111/1365-2664.13051, URL https://besjournals.onlinelibrary.wiley.com/doi/abs/10.1111/1365-2664.13051, https://besjournals.onlinelibrary.wiley.com/doi/pdf/10.1111/1365-2664.13051.

Salomonson, V. V., W. L. Barnes, P. W. Maymon, H. E. Montgomery, and H. Ostrow, 1989: MODIS: advanced facility instrument for studies of the Earth as a system. *IEEE Transactions on Geoscience and Remote Sensing*, **27 (2)**, 145–153, doi:10.1109/36.20292.

Saulquin, B., R. Fablet, A. Mangin, G. Mercier, D. Antoine, and O. Fanton d'Andon, 2013: Detection of linear trends in multisensor time series in the presence of autocorrelated noise: Application to the chlorophyll-a SeaWiFS and MERIS data sets and extrapolation to the incoming Sentinel 3-OLCI mission. *Journal of Geophysical Research: Oceans*, **118 (8)**, 3752–3763, doi:10.1002/jgrc.20264, URL https://agupubs.onlinelibrary.wiley.com/doi/abs/10.1002/jgrc.20264, https://agupubs.onlinelibrary.wiley.com/doi/pdf/10.1002/jgrc.20264.

Schulz, J., and Coauthors, 2009: Operational climate monitoring from space : the EUMETSAT Satellite Application Facility on Climate Monitoring (CM-SAF). *Atmospheric Chemistry And Physics*, **9 (5)**, 1687–1709, doi:10.5194/acp-9-1687-2009.

Traon, P.-Y. L., and Coauthors, 2015: Use of satellite observations for operational oceanography: recent achievements and future prospects. *Journal of Operational Oceanography*, **8 (sup1)**, s12–s27, doi:10.1080/1755876X.2015.1022050, URL https://doi.org/10.1080/1755876X.2015.1022050, https://doi.org/10.1080/1755876X.2015.1022050.

Voss, K., H. Gordon, S. Flora, B. Carol Johnson, M. Yarbrough, M. Feinholz, and T. Houlihan, 2017b: A method to extrapolate the diffuse upwelling radiance attenuation coefficient to the

surface as applied to the Marine Optical Buoy (MOBY). *Journal of Atmospheric and Oceanic Technology*, **34 (7)**, 1423–1432, doi:10.1175/JTECH-D-16-0235.1.

Wei, J., Z. Lee, M. Lewis, N. Pahlevan, M. Ondrusek, and R. Armstrong, 2015: Radiance transmittance measured at the ocean surface. *Opt. Express*, **23 (9)**, 11 826–11 837, doi:10.1364/OE.23.011826.

Zhao, M., F. A. Heinsch, R. R. Nemani, and S. W. Running, 2005: Improvements of the MODIS terrestrial gross and net primary production global data set. *Remote Sensing of Environment*, **95 (2)**, 164 – 176, doi:https://doi.org/10.1016/j.rse.2004.12.011, URL http://www.sciencedirect.com/science/article/pii/S0034425705000106.

Zibordi, G., 2006: Immersion factor of in-water radiance sensors: Assessment for a class of radiometers. *JOURNAL OF ATMOSPHERIC AND OCEANIC TECHNOLOGY*, **23 (2)**, 302–313, doi:10.1175/JTECH1847.1.

Zibordi, G., and B. Bulgarelli, 2007: Effects of cosine error in irradiance measurements from field ocean color radiometers. *Appl. Opt.*, **46 (22)**, 5529–5538, doi:10.1364/AO.46.005529.

Zibordi, G., and K. J. Voss, 1989: Geometrical and spectral distribution of sky radiance: Comparison between simulations and field measurements. *Remote Sensing of Environment*, **27 (3)**, 343 – 358, doi:https://doi.org/10.1016/0034-4257(89)90094-1, URL http://www.sciencedirect.com/science/article/pii/0034425789900941.

LIST OF TABLES

TABLE 1. Relative uncertainties $(k = 1)$ of the absolute radiometric calibration for the Satlantic 200-series radiometers used on the BOUSSOLE buoy. Uncertainties associated with the standards are shown first and then the uncertainty associated with using these standards for an absolute radiometric calibration at the NPL laboratory.

Wavelength [nm]	NPL irradiance standard	NPL irradiance calibration	Estimated Satlantic irradiance calibration	NPL reflectance standard	NPL radiance calibration	Estimated Satlantic radiance calibration
412	0.54 %	0.84 %	1.6 %	0.50 %	1.00 %	2.3 %
443	0.48 %	0.59 %	1.3 %	0.50 %	0.80 %	2.1 %
490	0.40 %	0.54 %	1.2 %	0.50 %	0.80 %	2.1 %
510	0.39 %	0.73 %	1.3 %	0.50 %	0.90 %	2.2 %
560	0.38 %	0.55 %	1.2 %	0.50 %	0.80 %	2.0 %
670	0.36 %	0.53 %	1.1 %	0.50 %	0.80 %	2.0 %
683	0.36 %	0.49 %	1.1 %	0.50 %	0.80 %	2.0 %

878 TABLE 2. Summary values of salinity, temperature and atmospheric pressure during the BOUSSOLE buoy
879 deployment under study.

Observed values	Mean	Median	Standard Deviation σ	Actual percentage coverage within 1 σ limits	Min- Max
Salinity in ‰	38.4	38.4	0.11	90 %	37.8-39.6
Water Temperature in °C	23.5	23.8	1.7	67 %	19.7-26.3
Air Temperature in °C	24.9	25.2	1.5	57 %	21.9-28.4
Atmospheric Pressure in mbar	1014.1	1014	3.2	77 %	1007-1024.6

TABLE 3. List of defined uncertainty sources.

Uncertainty source (contributor)	Directly Affected parameters	Uncertainty Evaluation type	Probability distribution shape
Radiance Absolute calibration k_{cal}	L_{u4}, L_{u9}	B	Normal
Irradiance Absolute calibration k_{cal}	E_s	B	Normal
Instrument Stability during deployment (included in k_{cal})	L_{u4}, L_{u9}, E_s	B	Rectangular
Diffuser Cosine response	E_s	B	Rectangular
Instrument random noise (statistics of 1 minute raw signal)	L_{u4}, L_{u9}, E_s	A	Normal
Wave focusing (statistics of 1 minute raw signal)	L_{u4}, L_{u9}	A	Normal
Depth (derived from a separated model with several uncertainty sources)	z_4, z_9, f_{tilt}	B	Normal
Solar Zenith Angle	k_{cos}, f_s, f_{tilt}	B	Rectangular (k_{cos}, f_s), Normal (f_{tilt})
Chlorophyll concentration	f_s, f_h	B	Rectangular (f_s), Normal(f_h)
Clear sky irradiance model	f_{dir}	B	Rectangular
Air- water transmission	$C_{\rho n}$	B	Normal

TABLE 4. SVC quality selection criteria used for the BOUSSOLE data set.

Selection criteria	
One minute readings stability	< 2 %
Clear sky test	$0.9 < \& > 1.1$
Tilt	$< 10^{\circ}$
SZA	$< 75^{\circ}$
Depth	< 11 m
Shading	< 5 %
Bio fouling	N
Screening for inter calibration issue	Passed

TABLE 5. Uncertainty budget of Satlantic 200-radiometers deployed onto the BOUSSOLE buoy $(k = 1)$.

Wavelength [nm]	E_s	L_{u_4}	L_{u0^-}	L_w	R_{rs}
412	2.29 %	2.40 %	2.96 %	3.14 %	3.86 %
443	2.11 %	2.40 %	2.95 %	3.04 %	3.68 %
490	2.16 %	2.40 %	2.94 %	3.02 %	3.70 %
510	2.17 %	2.49 %	3.01 %	3.09 %	3.77 %
560	2.20 %	2.40 %	2.93 %	3.02 %	3.73 %
670	2.23 %	2.43 %	3.03 %	4.38 %	4.88 %
683	2.17 %	2.78 %	3.78 %	4.90 %	5.35 %

LIST OF FIGURES

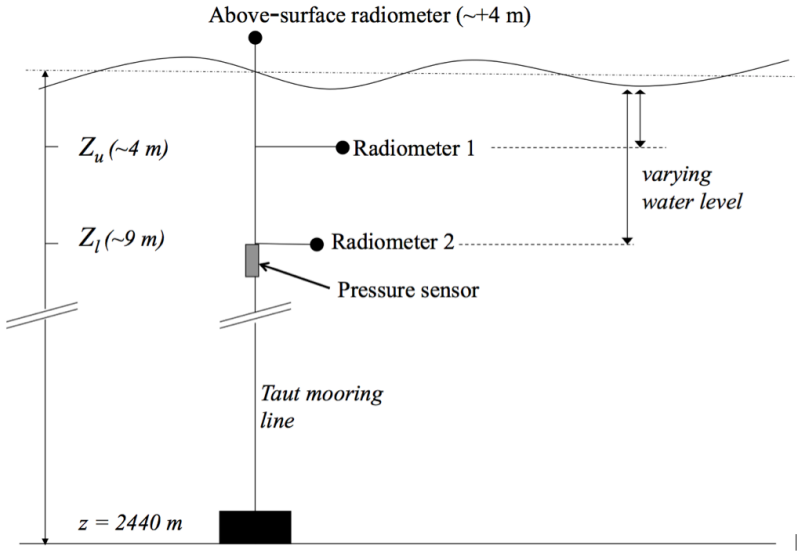

FIG. 1. Schematic layout of how the BOUSSOLE radiometers are installed on the buoy.

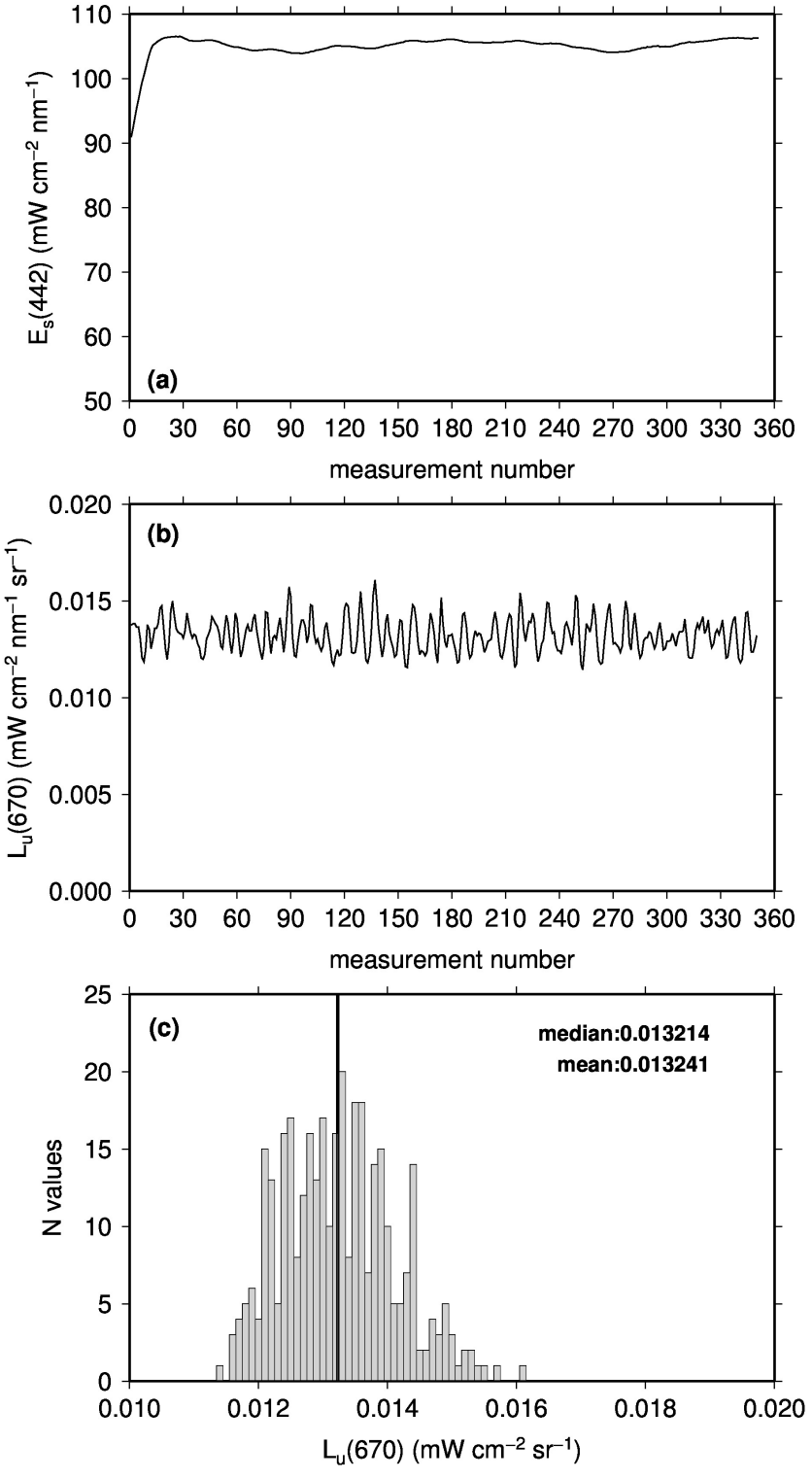

915 FIG. 2. Examples of one-minute time series of data acquisition for (a) E_s at 442 nm, (b) L_u at 670 nm. The
916 distribution of the data in (b) is shown in (c).

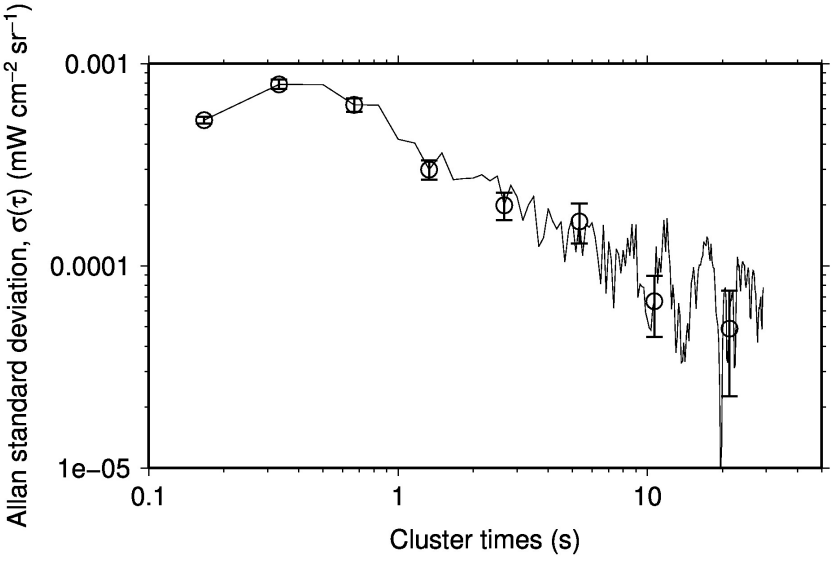

FIG. 3. Allan deviation one-minute time series of data acquisition for L_u at 670 nm.

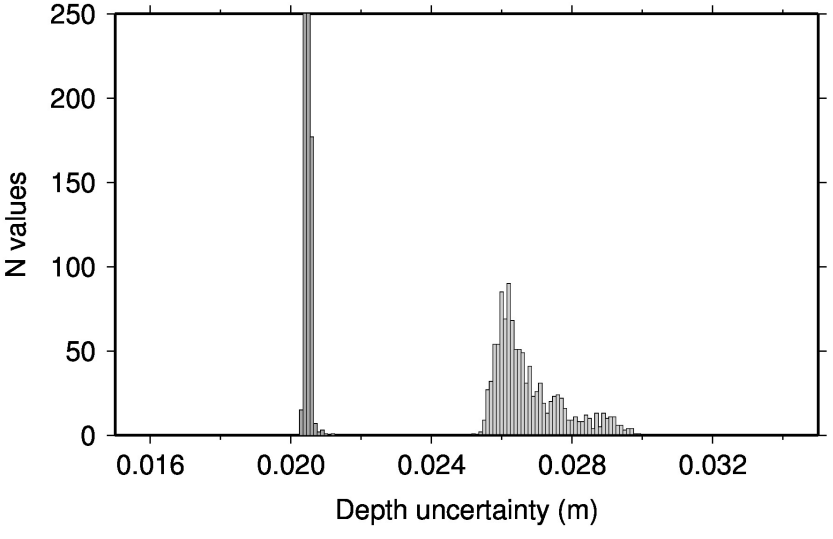

FIG. 4. Uncertainty in the measurement depth for the deepest (light grey) and shallowest (dark grey) buoy arms.

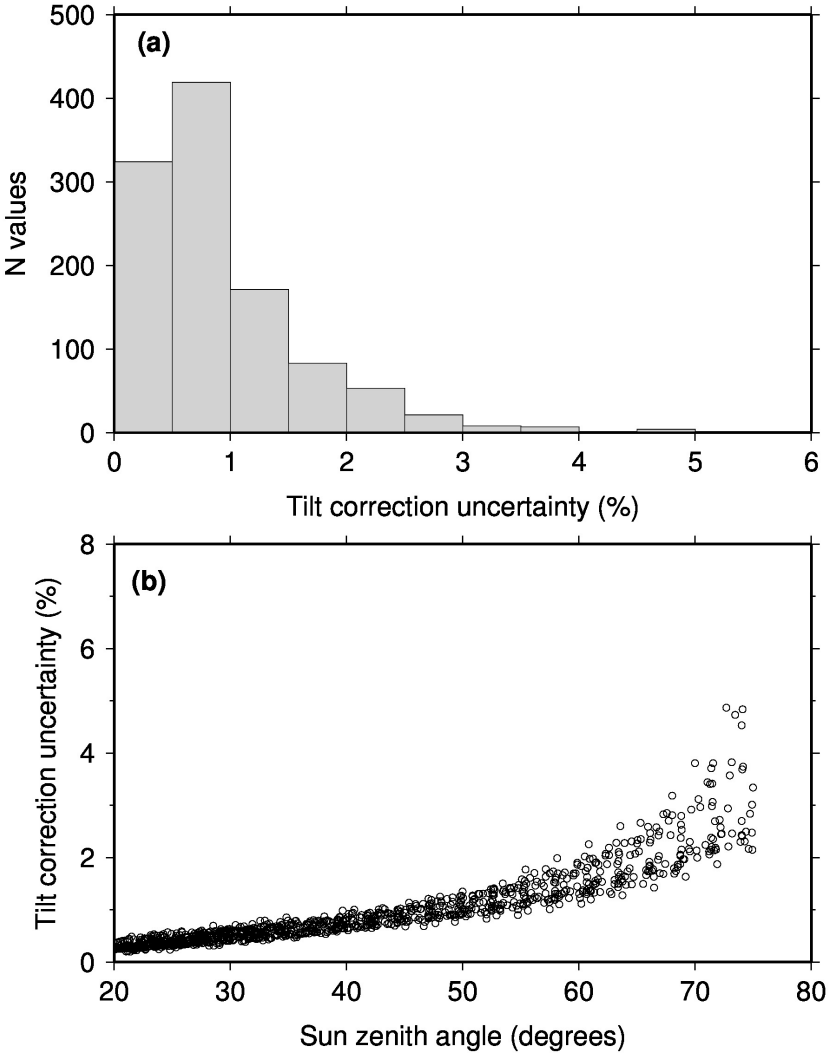

FIG. 5. (a) Distribution of the uncertainty in the tilt correction applied to the E_s measurement and, (b) its change as a function of the sun zenith angle.

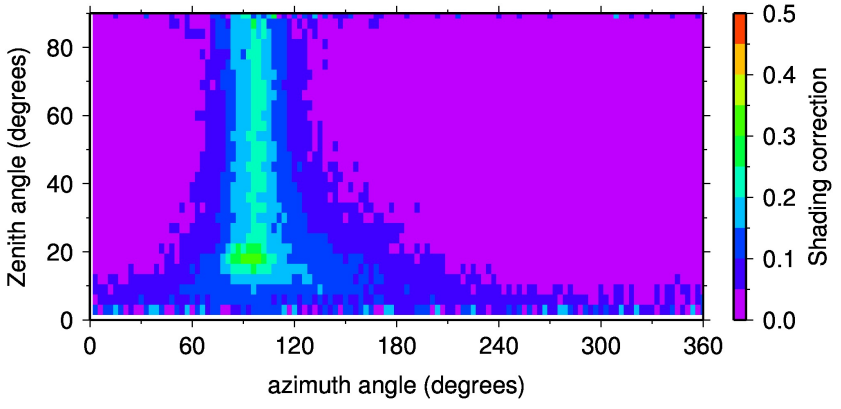

FIG. 6. Example of the shading correction, here for L_{u4} at 510 nm, for a chlorophyll concentration of 0.1 mg(Chl) m^{-3}.

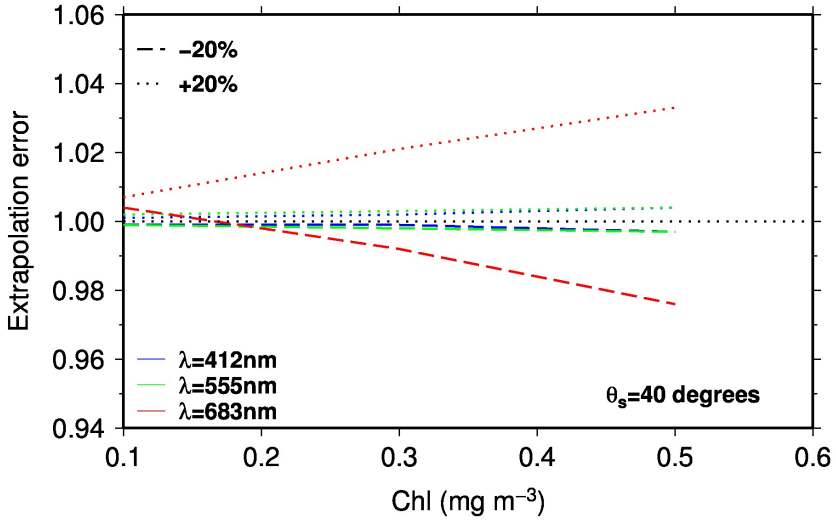

921 FIG. 7. Changes of the extrapolation correction as a function of the chlorophyll concentration, when the input
922 concentration is changed by ± 20 % and for the wavelengths indicated.

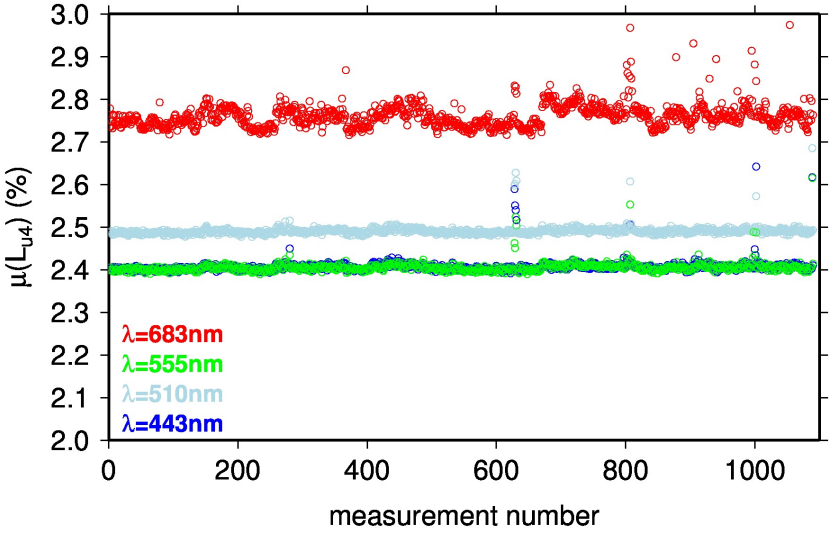

FIG. 8. Relative uncertainty in L_{u4}, $(k = 1)$, for the four wavelengths indicated.

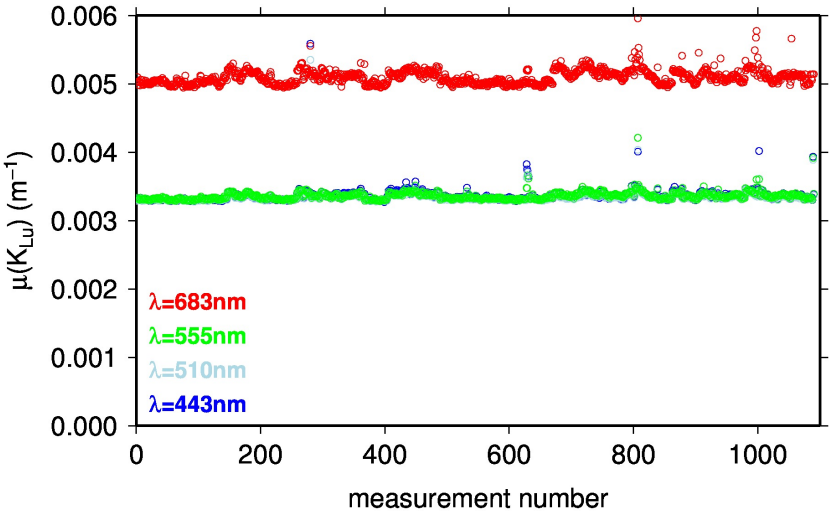

FIG. 9. Absolute uncertainty in K_{Lu}, $(k = 1)$, for the four wavelengths indicated.

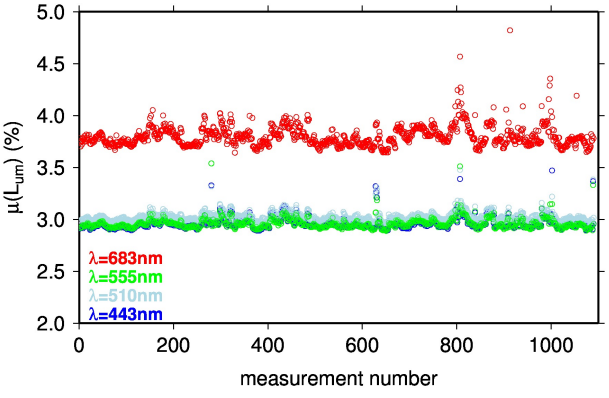

FIG. 10. Relative uncertainty in $L_{\mathrm{u}}(0^{-}),\ (k=1)$, for the four wavelengths indicated.

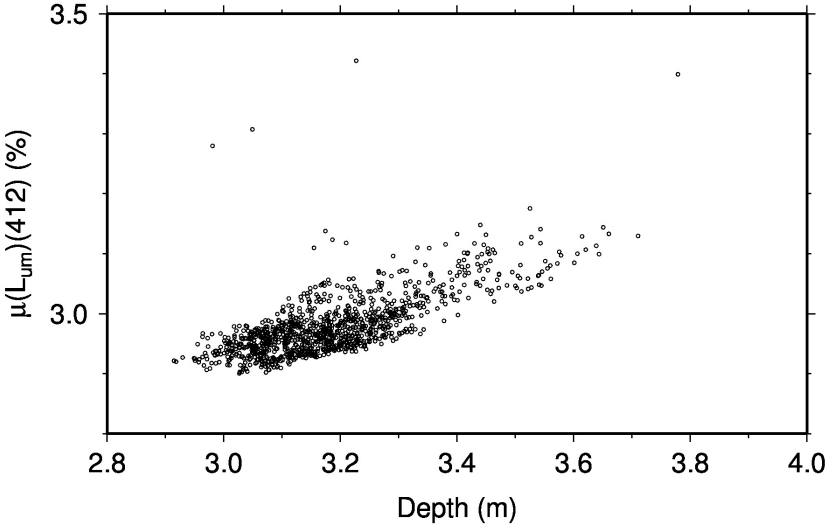

923 FIG. 11. Relative uncertainty in $L_u(0^-)$, $(k = 1)$, at 412 nm as a function of the actual depth of the shallowest
924 arm.

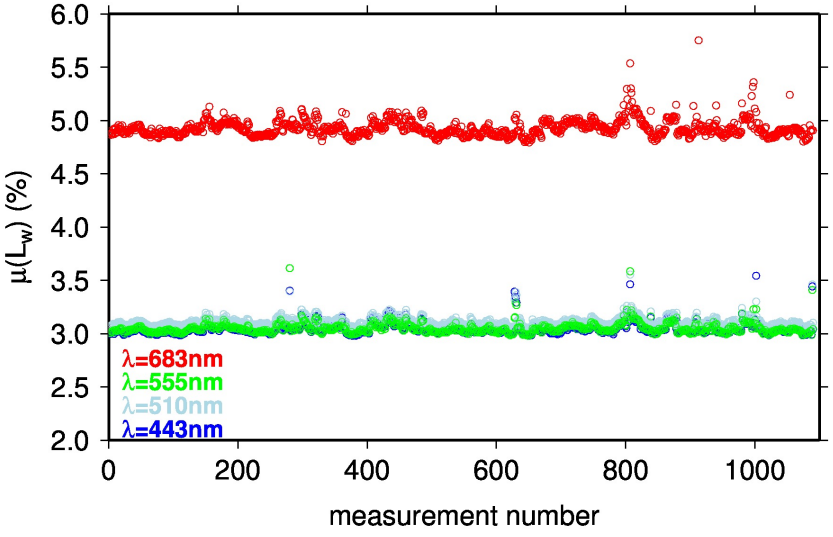

FIG. 12. Relative uncertainty in L_{w}, $(k = 1)$, for the four wavelengths indicated.

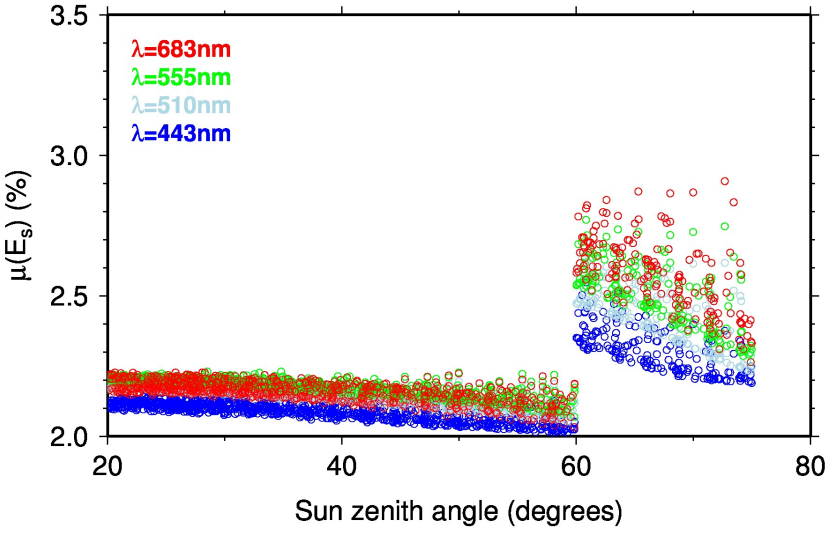

925 FIG. 13. Relative uncertainty in E_s, $(k = 1)$,as a function of the sun zenith angle, for the four wavelengths
926 indicated.

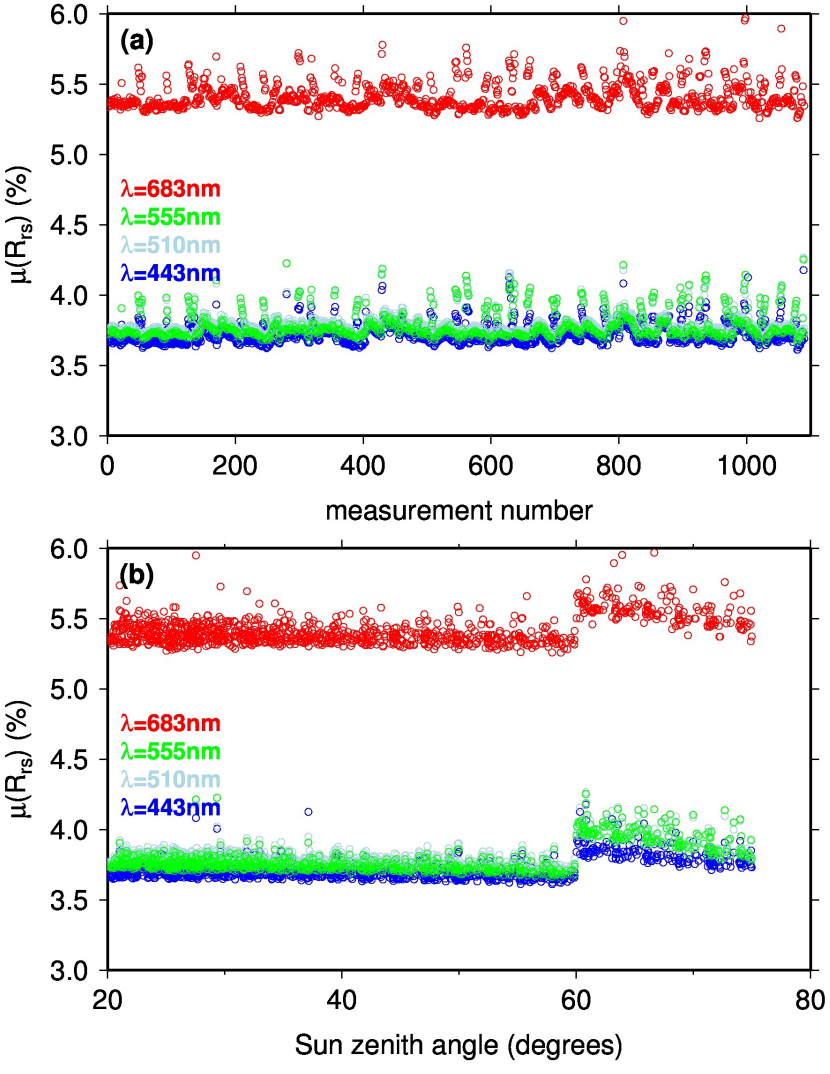

927 FIG. 14. (a) Relative uncertainty in R_{rs}, $(k = 1)$, for the four wavelengths indicated, and (b) the same data as
928 in (a) plotted as a function of the sun zenith angle.

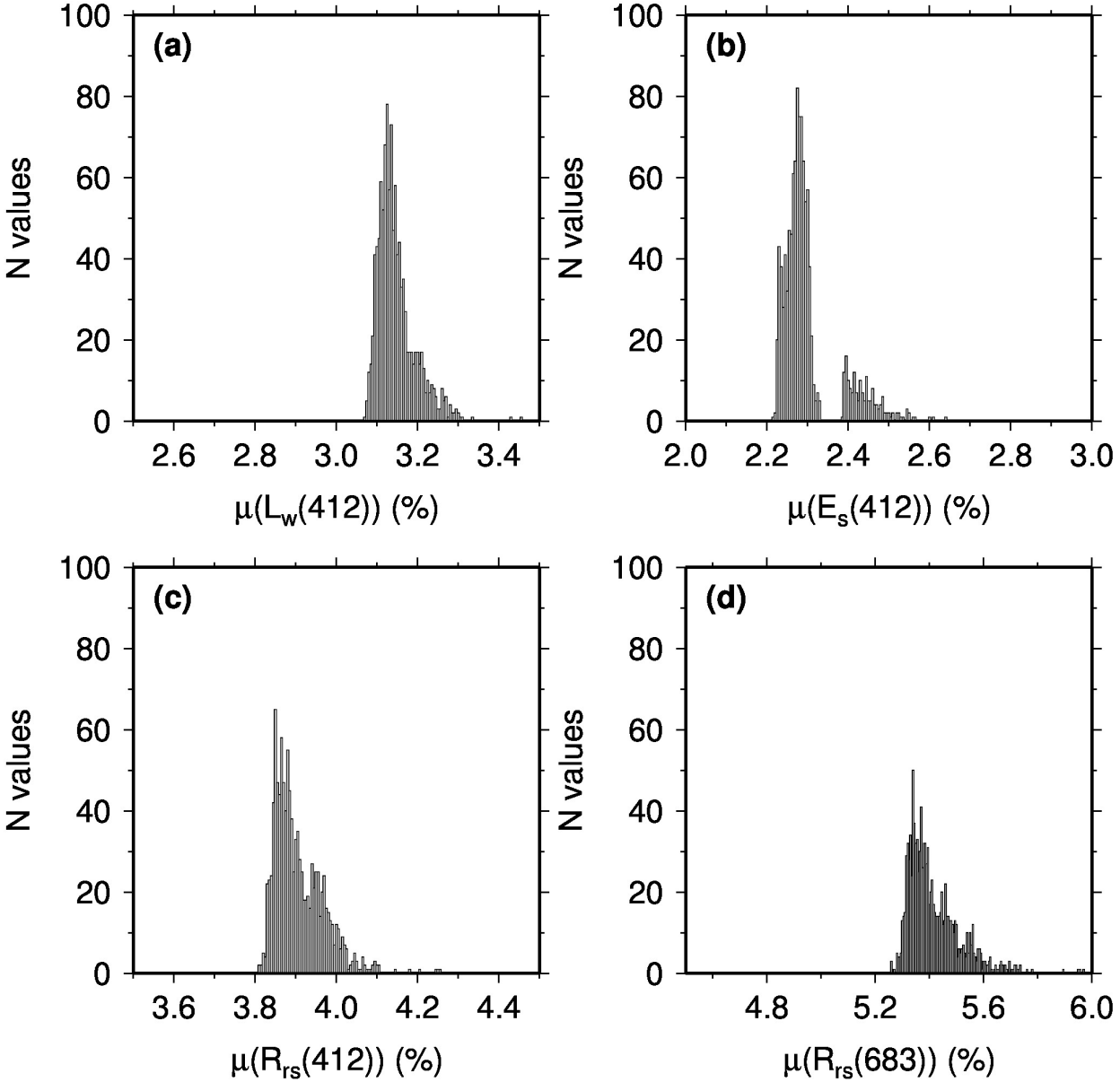

FIG. 15. Example distributions of relative uncertainties ($k = 1$) for the parameters and wavelengths indicated.

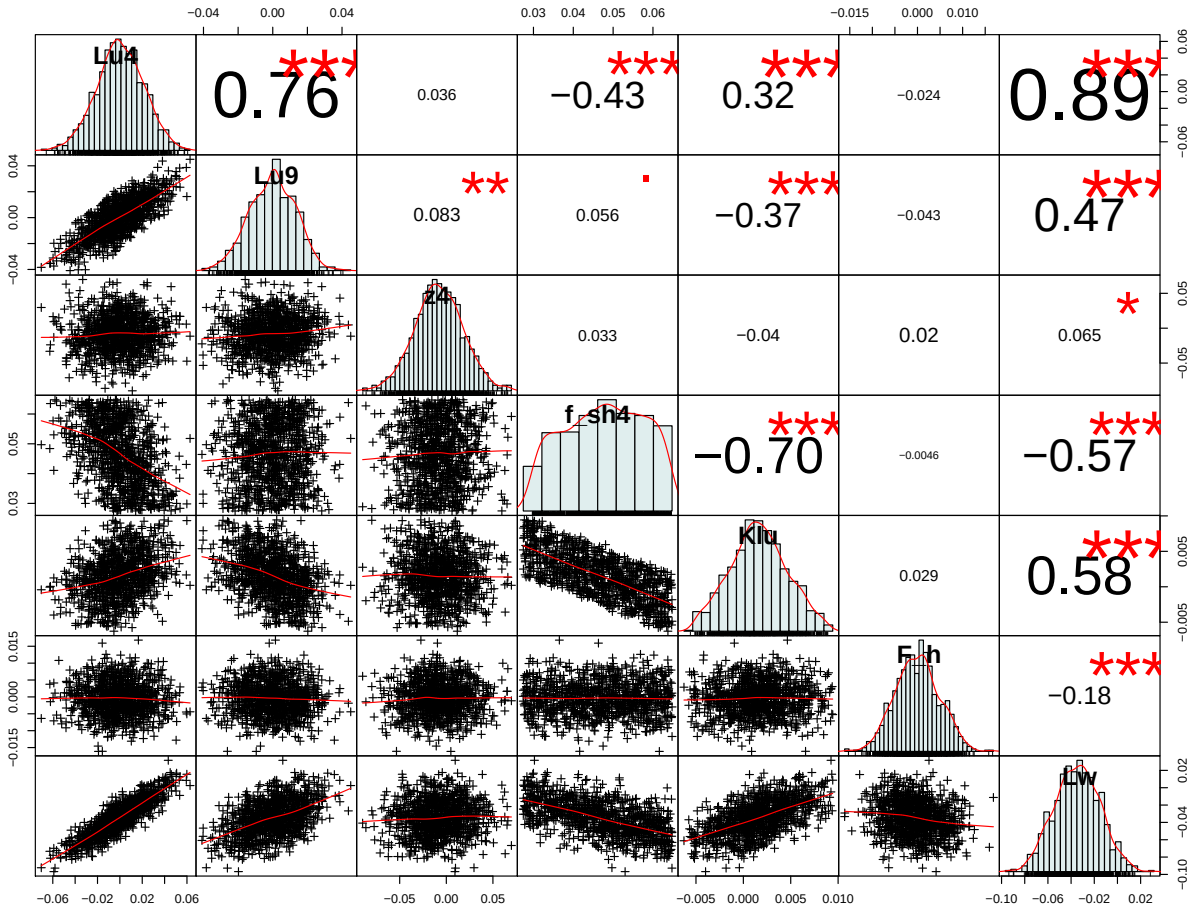

Fig. A1. Error correlation for 412 nm input components for L_w. The variables presented in columns are L_{u4} the upwelling radiance at 4 m depth, L_{u9} the upwelling radiance at 9 m depth, z4 the depth at upper arm, f_{sh4} the shading correction fpr upper arm, K_{Lu} the diffuse attenuation coefficient for upwelling radiance, f_h the Hydrolight-based extrapolation correction, and L_w the waterleaving radiance.

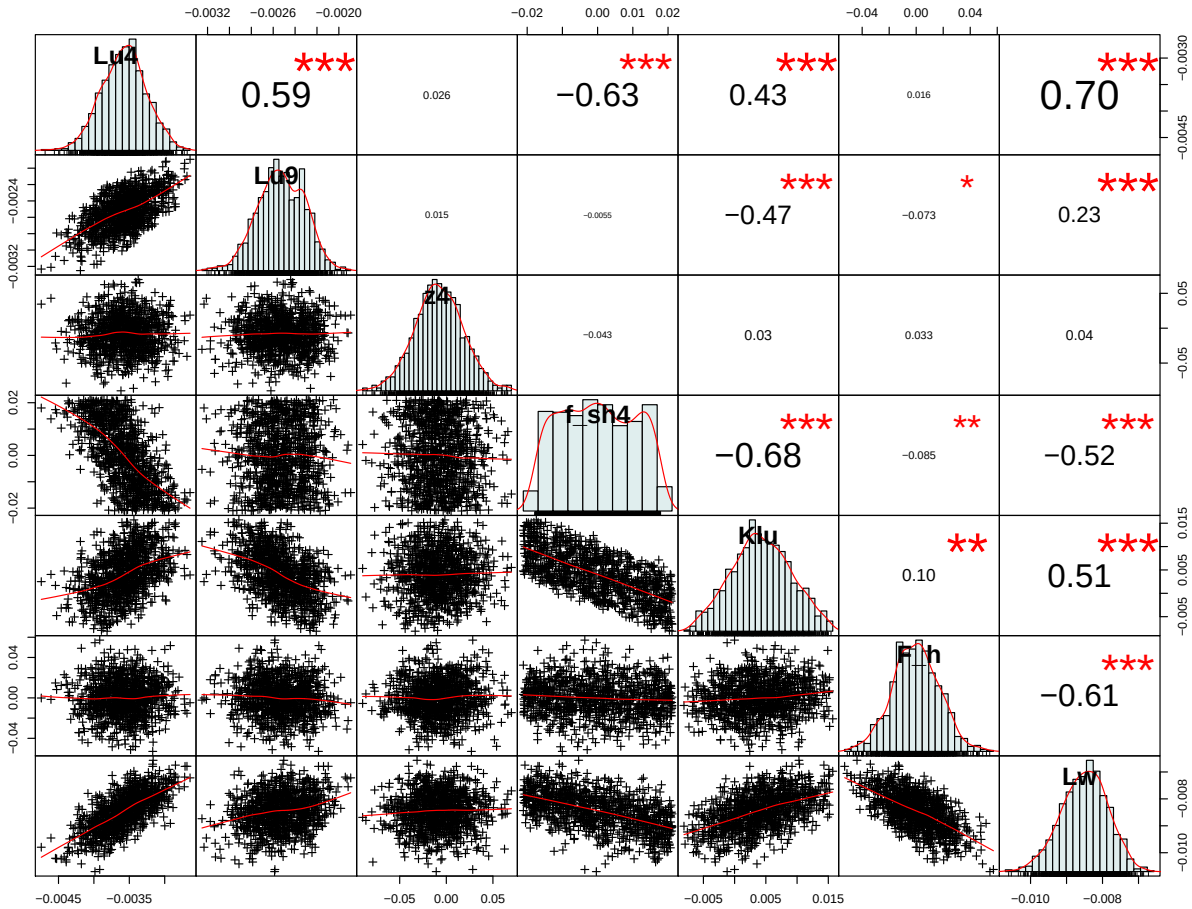

933 Fig. A2. Error correlation for 683 nm input components for L_{w}. The variables presented in columns are
934 L_{u4} the upwelling radiance at 4 m depth, L_{u9} the upwelling radiance at 9 m depth, z4 the depth at upper arm,
935 f_{sh4}-the shading correction fpr upper arm, $K_{L\mathrm{u}}$ the diffuse attenuation coefficient for upwelling radiance, f_h the
936 Hydrolight-based extrapolation correction, and L_{w} the waterleaving radiance.